J. Fluid Mech. (2008), *vol.* 611, *pp.* 61–95.
doi:10.1017/S0022112008002449 Printed in the United Kingdom

Interharmonics in internal gravity waves generated by tide-topography interaction

ALEXANDER S. KOROBOV AND KEVIN G. LAMB

Department of Applied Mathematics, University of Waterloo, Waterloo, Canada

(Received 12 March 2007 and in revised form 16 May 2008)

The dynamics and spectrum of internal gravity waves generated in a linearly stratified fluid by tidal flow over a flat-topped ridge are investigated at five different latitudes using an inviscid two-dimensional numerical model. The resulting wave field includes progressive freely propagating waves which satisfy the dispersion relation, and forced waves which are trapped non-propagating oscillations with frequencies outside the internal wave band. The flow is largely stable with respect to shear instabilities, and, throughout the runs, there is a negligibly small amount of overturning which is confined to the highly nonlinear regions along the sloping topography and where tidal beams reflect from the boundaries. The wave spectrum exhibits a self-similar structure with prominent peaks at tidal harmonics and interharmonics, whose magnitudes decay exponentially with frequency. Two strong subharmonics are generated by an instability of tidal beams which is particularly strong for near-critical latitudes where the Coriolis frequency is half the tidal frequency. When both subharmonics are within the free internal wave range (as in cases 0°–20° N), they form a resonant triad with the tidal harmonic. When at least one of the two subharmonics is outside of the range (as in cases 30°–40° N) the observed instability is no longer a resonant triad interaction. We argue that the two subharmonics are generated by parametric subharmonic instability that can produce both progressive and forced waves. Other interharmonics are produced through wave–wave interactions and are not an artefact of Doppler shifting as assumed by previous authors. As the two subharmonics are, in general, not proper fractions of the tidal frequency, the wave–wave interactions are capable of transferring energy to a continuum of frequencies.

1. Introduction

A periodic disturbance in a stably, continuously stratified fluid generates a response across a wide range of frequencies. This can consist of progressive waves which propagate away from the generation site, or non-propagating forced waves, which remain trapped at their generation site. In the case of finite-amplitude disturbances, the generation process and the resulting fluid motion are usually too complex to be described directly in terms of particle displacements or velocities. However, there is evidence that the spectrum of the wave field has a much simpler structure which allows insight into the nature of the flow. The deep ocean, for example, abounds with internal waves, generated primarily by tides and winds (Munk & Wunsch 1998); the variety and multitude of factors that affect the internal wave field make a direct description of the waves impossible. Yet, the energy spectrum of the waves has a simple algebraic representation, known as the Garrett–Munk spectrum (Garrett & Munk 1975), which is universal throughout the deep ocean away from the strong generation

sites. With this in mind, in order to understand the essential physics of a flow generated by a periodic disturbance, the fluid dynamics may be studied in association with the energy transfers within the spectrum (see, for example, Winters & D'Asaro 1997; Hibiya, Niwa & Fujiwara 1998; Furue 2003; Furuchi, Hibiya & Niwa 2005; Gerkema, Staquet & Bouruet-Aubertot 2006; Legg & Huijts 2006; MacKinnon & Winters 2007).

Apart from being a potentially efficient approach to describing the complex phenomenon, the internal wave spectrum provides insight into energy transfers within the internal wave field, which has important applications in several areas including climate change and nutrient cycles. The reason why energy transfers among internal waves affect these such seemingly unrelated processes is due to the connection of internal waves to deep-ocean mixing (Garrett 2003). Mixing in the deep ocean conveys heat from the upper layer of the ocean to the abyssal cold waters, and, thus, helps maintain the meridional overturning circulation. The role of internal waves is to transfer energy from the primary sources of oceanic mechanical energy, i.e. from tides and winds, to mixing (Dewar *et al.* 2006 suggests that the marine biosphere is another important source of energy for mixing). This makes internal waves much more than a background noise in the medium: internal waves are an important dynamical part of global processes in the ocean, including climate change and nutrient cycles. The significance of internal waves in connection to deep-ocean mixing was realized at the earliest stage of internal wave research (Sverdrup, Johnson & Fleming 1942); however, knowledge of the energy cascade in internal waves is far from complete.

Nevertheless, many facts about the energy cascade in internal waves are known. The first one is rather obvious: if the oscillating source has frequency ω_0 and the excursion distance is small so that no lee waves are generated, most of the internal waves generated directly by the source have frequency ω_0. Consequently, a considerable amount of energy may be put into progressive waves of frequency ω_0.

Historically, the presence of a dominant frequency was the first property of internal waves to be noticed. For example, in 1907, not long after the discovery of internal waves in the ocean by Nansen (1902), Otto Pettersson discovered the tidal periodicity of vertical internal movements in Danish sounds; this was important, as tides were not known as a source of internal waves at that time.

Internal waves of the fundamental frequency were also the target of the earliest experimental studies. For example, Görtler (1943), Mowbray & Rarity (1967), Thorpe (1968) and many others, observed internal wave beams of the fundamental frequency generated by a body oscillating in a linearly stratified fluid. In the special case of linear stratification, when the buoyancy frequency N_b and Coriolis frequency f are constant, the beam of frequency $\omega \in (f, N_b)$ has constant slope r given by

$$r^2 = \frac{\omega^2 - f^2}{N_b^2 - \omega^2}, \tag{1.1}$$

and internal waves are manifested in the famous St Andrew's cross pattern. Oceanic analogues, topographically generated beams of tidal frequency, can be found in numerical studies (e.g. Holloway & Merrifield 1999), and in several field observations (Pingree & New 1991; Carter, Gregg & Merrifield 2006; Rainville & Pinkel 2006). However, the best confirmation of the fact that waves of the fundamental frequency represent the first candidate to drain energy from the source comes from the spectra of internal waves. In the deep ocean, for example, the spectra of internal waves near rough topography and near the surface are often characterized by prominent

peaks at the tidal and Coriolis frequencies (Olbers 1983), these being the fundamental frequencies of the two sources.

Waves of the fundamental frequency ω_0 generated by an oscillating source are usually accompanied by weaker waves of higher harmonics $n\omega_0$, where $n \in \{2, 3, \ldots\}$. Although the harmonics have been observed in experiments (e.g. Mowbray & Rarity 1967), their nature and energetics were obscure until the work by Bell (1975). He considered a linearly stratified tidal flow over isolated topography in a non-rotating fluid of infinite depth, and used the first-order approximation of the nonlinear operator in the governing equations. Bell's solution was later extended to the case of finite depth by Khatiwala (2003). The solutions obtained by Bell and Khatiwala are given by linear superpositions of tidal harmonics emanating from near the ridge; the energy in harmonics $n\omega_0$ decays rapidly with n. It was realized later that harmonics may also be produced by higher-order nonlinear interactions at locations where waves of harmonic frequencies cross. The generation of the higher harmonics through the collision or reflection of internal wave beams can be found in the numerical experiments by Lamb (2004) and Gerkema *et al.* (2006) and in laboratory experiments (Peacock & Tabaei 2005; Zhang, King & Swinney 2007). There are also field observations where internal waves are generated by nonlinear superposition of tidal harmonics (Stashchuk & Vlasenko 2005). The fact that the interaction of internal wave beams can generate harmonics inspired a theoretical investigation of the nonlinear interactions (Tabaei, Akylas & Lamb 2005). On the whole, there is plenty of evidence that the harmonics represent a family of frequencies that can efficiently receive energy from the source and transfer it to other waves.

As internal waves are intrinsically unstable (Drazin 1977; Koudella & Staquet 2006), the set of possible frequencies is not limited to harmonics only. In weakly nonlinear theory, when a single internal wave of frequency ω_0 and wave vector $\boldsymbol{K}_0$ is subjected to a small perturbation, an instability of parametric subharmonic type will inevitably set in, and the primary wave will decay into two small-scale waves of about half the frequency. This process, known as the parametric subharmonic instability (PSI), represents an important class of resonant triad interactions. A resonant triad interaction implies three waves with wave vectors and frequencies $(\boldsymbol{K}_j, \omega_j)$ for $j = 0, 1, 2$, each of which satisfies the dispersion relation $k_h/m = \pm r$ where k_h is the horizontal wavenumber, m is the vertical wavenumber and r is the slope of the group velocity vector given by (1.1), and for which $\boldsymbol{K}_0 + \boldsymbol{K}_1 + \boldsymbol{K}_2 = 0$ and $\omega_0 + \omega_1 + \omega_2 = 0$ (Phillips 1977). In particular, all three waves are freely propagating. Hasselman (1967) showed that in a resonant triad, the wave with the highest absolute frequency is unstable to the other two waves. Thus the initial wave 0 is unstable provided $|\omega_0| = |\omega_1| + |\omega_2|$. The maximum growth rate occurs for $\omega_1 = \omega_2 = \omega_0/2$ in the limit of high wavenumbers $|\boldsymbol{K}_1| \sim |\boldsymbol{K}_2| \gg |\boldsymbol{K}_0|$ (Staquet & Sommeria 2002). PSI was first observed for standing internal waves in the laboratory experiments by Thorpe (1968) and McEwan (1971). Early numerical studies on PSI within an oceanic context were reviewed by Orlanski (1981).

PSI, along with other resonant triad interactions, occurring in a random internal wave field, is too slow to be the dominant mechanism for energy transfers in the deep ocean (Olbers & Pomphrey 1981). Two factors can increase the transfer rate, both of which occur at the generation site: stronger nonlinearity and coherence among the waves. As the flow changes from weakly nonlinear to strongly nonlinear (and internal waves in the ocean are strongly nonlinear, according to Holloway 1980), PSI turns into a strong rapid instability whose properties are somewhat different from the picture provided by weakly nonlinear theory. The link between the weakly nonlinear and

strongly nonlinear regimes remains poorly understood (Staquet & Sommeria 2002). As the nonlinearity strengthens, the time scales associated with PSI decrease (de Silva, Imberger & Ivey 1997; MacKinnon & Winters 2007). The regions where strong rapid nonlinear instabilities may occur include regions of reflection of an internal wave beam from the boundary (Javam, Imberger & Armfield 1999) and regions where two strong beams intersect (McEwan 1973; Teoh, Ivey & Imberger 1997; Javam, Imberger & Armfield 2000). The strong subharmonics observed in numerical simulations of internal tides by MacKinnon & Winters (2003), Lamb (2004) and Gerkema *et al.* (2006) are also generated by strong rapid nonlinear instabilities. Strong coherence among the interacting waves further strengthens the nonlinear interaction in these sites. It is likely that the strong subharmonics seen in field observations (e.g. Carter & Gregg 2006) are also the result of strongly nonlinear instabilities.

In this paper we provide evidence that PSI generates subharmonics whose frequencies are in general different from $\omega_0/2$ and depend on latitude. When the subharmonics are within the free internal wave range, they form a resonant triad with the tidal harmonic ω_0. However, the subharmonics generated by PSI are not restricted to progressive internal waves only: for supercritical latitudes, the subharmonic frequencies fall out of the free internal wave range, and the waves generated by the instability become forced. Thus, in the fully nonlinear case, PSI does not necessarily have to be a resonant triad interaction. This is an important result as transferring energy into forced locally trapped waves can have a great impact on mixing (Teoh *et al.* 1997; Javam *et al.* 1999, 2000).

If there are several sources of internal waves with fundamental frequencies $\omega_1, \omega_2, \ldots$, strong waves can be generated at the combination frequencies, such as $|\omega_1 - \omega_2|$, $|2\omega_1 - \omega_2|$, $|2\omega_2 - \omega_1|$, etc. The waves at combination frequencies are generated by triad interactions, which do not have to be resonant. This was studied experimentally (Teoh *et al.* 1997; Chashechkin & Nekludov 1990), theoretically (Kistovich & Chashechkin 1991), and numerically (Javam *et al.* 2000). Strong waves at combination frequencies have been observed in the ocean (van Haren, Maas & van Aken 2002).

If strong internal waves of fundamental frequency ω_0 are subjected to a subharmonic instability generating energetic waves at two frequencies ω_1, ω_2 with $|\omega_1|, |\omega_2| \in (0, |\omega_0|)$, then the subharmonic instability is followed by the generation of oscillations at all combination frequencies of ω_0, ω_1 and ω_2, including freely propagating and forced waves. If the generated subharmonics are not proper fractions of ω_0, energy fed into the fundamental frequency may spread throughout the whole continuum of frequencies comprised of all combination frequencies. Typically, nonlinearly interacting waves lose only a small fraction of their energy toward newly generated waves. This leads to an energy cascade: strong waves give away a little of their energy to their descendants, and the descendants, in their turn, produce more waves, which are even less energetic. In this paper, we look into several particular realizations of this sort of energy cascade.

We model internal wave dynamics of a tidal flow over an idealized topography and investigate the spectral content of the flow. We show that apart from the harmonics and subharmonics, waves of interharmonic frequencies greater than the fundamental frequency are generated. Interharmonics are defined as frequencies lying between the multiples of the fundamental frequency; subharmonics are a subclass of interharmonics with frequencies less than the fundamental frequency. Subharmonics are generated by the instability of the tidal beam near strongly nonlinear regions. Through wave–wave interactions, energy transfers from subharmonics to higher interharmonics, so that the interharmonic frequencies observed in the flow spectra

happen to be the combination frequencies of the strongest subharmonics and harmonics.

The paper is organized as follows. In § 2, we describe the framework that we used: physical assumptions, governing equations with corresponding boundary conditions and the geometry of the domain. Methods employed to investigate the problem are described in § 3. In particular, we describe the numerical model solving the governing equations, the data that we analysed and the spectral analysis techniques. The results are presented in § 4. There, we explain the underlying dynamics of the observed energy transfers and present spectral analysis of the flow.

2. Framework

2.1. *Assumptions*

In order to model internal wave dynamics, we have made several assumptions, which fall into three categories: (i) assumptions concerning the domain under study; (ii) assumptions on fluid properties; (iii) approximations concerning the Earth's rotation.

The most restrictive assumption is the two-dimensionality of the flow. It does, however, have the advantage that use of a two-dimensional model allows much higher resolution than could be achieved with a three-dimensional one. Another restriction on the domain is the rigid-lid approximation where we assume that the movement of the surface is negligibly small. As the depth of the domain is 5 km and oscillations of the surface associated with internal waves are typically of the order of a few centimetres, the dynamics of the flow is not significantly modified by use of the rigid-lid approximation.

For simplicity of interpretation of the results, we assume that the fluid is incompressible, inviscid and linearly stratified. In addition, the traditional f-plane approximation is used, i.e. the Coriolis frequency is assumed constant throughout the domain. The last approximation that we use is the Boussinesq approximation, i.e. the density variations are assumed negligible in every term of the governing equations except for the gravity term. The Boussinesq approximation is very good for the ocean (see, for example, Kundu & Cohen 2002), and it also facilitates the solving of the governing equations. The assumption of a linearly stratified fluid under the Boussinesq approximation means that internal wave beams remain coherent indefinitely as the phase speed of a mode-n wave is inversely proportional to the mode number. For more realistic stratifications, e.g. those with a strong thermocline as observed in the ocean, internal wave beams rapidly disappear once they reach the thermocline as the phase speeds of the various modes are no longer commensurate. Thus, in reality, the pattern of coherent internal wave beams observed in our simulations throughout the domain would not exist far away from the topography. For example, Martin, Rudnick & Pinkel (2006) investigating the Hawaiian Ridge of height more than 3 km, did not observe any beam patterns further than 100 km from the ridge.

2.2. *Governing equations*

Under the assumptions described in the previous section, the equations governing internal wave dynamics are the two-dimensional incompressible Euler equations under the Boussinesq approximation (Lamb 1994):

$$\left.\begin{array}{c} \boldsymbol{u}_t + \boldsymbol{u}\cdot\nabla\boldsymbol{u} + f\boldsymbol{k}\times\boldsymbol{u} = -\nabla p - \rho g\boldsymbol{k}, \\ \rho_t + \boldsymbol{u}\cdot\nabla\rho = 0, \\ \nabla\cdot\boldsymbol{u} = 0. \end{array}\right\} \tag{2.1}$$

Here, $\nabla = (\partial/\partial x, 0, \partial/\partial z)$ and the unit vector in the z-directionis $\boldsymbol{k} = (0, 0, 1)$.

In (2.1), there are three unknowns depending on time t and spatial coordinates x and z: the velocity vector $\boldsymbol{u}=(u, v, w)$; the normalized density perturbation ρ, such that physical density ρ_{ph} is given by $\rho_{ph}=\rho_0(1+\rho)$, where ρ_0 is taken to be the surface density; and the normalized pressure p related to the physical pressure p_{ph} by the formula $p_{ph}=p_{atm}+\rho_0(p-gz)$, where p_{atm} is the atmospheric pressure. Equations (2.1) have two parameters: the Coriolis frequency f related to the latitude θ by the formula $f=2\Omega\sin(\theta)$, where $\Omega\approx 0.73\times 10^{-4}\,\mathrm{s}^{-1}$ is the angular velocity of the Earth, and the acceleration due to gravity $g=9.81\,\mathrm{m\,s}^{-1}$.

Equations (2.1) are solved in a symmetric two-dimensional domain representing a vertical cross-section of the ocean with a flat-topped ridge at the bottom:

$$R=\{(x,z)\parallel -L/2\leqslant x\leqslant L/2,\ -H+h(x)\leqslant z\leqslant 0\},$$

where L is the horizontal length of the domain, H is the water depth away from the ridge, and $h(x)$ defines the topography of the ocean bottom. In this work, the shape of the topography was given by

$$h(x)=A\exp\left[-\left(\frac{x}{d}\right)^4\right], \tag{2.2}$$

with $A=1800\,\mathrm{m}$ being the amplitude and $d=12500\,\mathrm{m}$ defining the width of the ridge. The hill $h(x)$ is supercritical, i.e. its maximum slope is steeper than the slope r_0 of the radiated internal tide. The criticality parameter corresponding to the topography is defined as $\alpha=\max(h'(x))/r_0$ and is within the range $[1.54, 2.07]$ for the considered cases. With respect to the second harmonic, the topography is subcritical in all cases, i.e. $\max(h'(x))/r_2\in[0.75, 0.79]$, where r_2 is the slope corresponding to the second harmonic at one of the five latitudes. The parameters associated with the domain description are summarized in table 1 along with other parameters. The development of the fluid flow is considered on the time domain $[0, T_{tot}]$, where $T_{tot}=30\,\mathrm{days}$.

The governing equations (2.1) are subject to boundary conditions at each side of the domain and an initial condition. At the left-hand boundary the flow is forced with a periodic tidal current $U(t)=U_0\cos(\omega_0 t)$. The following typical values for the amplitude U_0 and the semidiurnal tidal frequency ω_0 were used: $U_0=0.025\,\mathrm{m\,s}^{-1}$ and $\omega_0=1.4075\times 10^{-4}\,\mathrm{s}^{-1}$. At the bottom of the domain, an impermeability condition is imposed: $\boldsymbol{u}\cdot\boldsymbol{n}=0$, where $\boldsymbol{n}$ is a vector normal to the boundary. At the top of the domain, we also use the impermeability condition $w=0$. At the right-hand boundary, an outflow boundary condition is applied, allowing long waves to propagate away freely without reflection. The model is initialized with the peak rightward barotropic flow: $u(x, z, t=0)=Q/[H-h(x)]$, and $v(x, z, t=0)=0$, where Q is the maximum barotropic volume flux given by $Q=U_0H$. Incompressibility then dictates the vertical velocity component: $w(x, z, t=0)=-Qh'(x)z/(H-h(x))^2$. The fluid density at time $t=0$ is linearly stratified, so that the buoyancy frequency

$$N_b\equiv\left(-\frac{g}{\rho_0}\frac{\mathrm{d}\rho_{ph}}{\mathrm{d}z}\right)^{1/2}=10^{-3}\,s^{-1} \tag{2.3}$$

is constant.

Category	Parameter	Value
Physical	Coriolis frequency	$f(\theta = 0°) = 0\,\mathrm{s}^{-1}$
		$f(\theta = 10°) = 0.2535 \times 10^{-4}\,\mathrm{s}^{-1}$
		$f(\theta = 20°) = 0.4993 \times 10^{-4}\,\mathrm{s}^{-1}$
		$f(\theta = 30°) = 0.7300 \times 10^{-4}\,\mathrm{s}^{-1}$
		$f(\theta = 40°) = 0.9385 \times 10^{-4}\,\mathrm{s}^{-1}$
	Maximum tidal speed (deep water)	$U_0 = 0.025\,\mathrm{m\,s}^{-1}$
	Tidal frequency	$\omega_0 = 1.4075 \times 10^{-4}\,\mathrm{s}^{-1}$
	Tidal excursion distance (deep water)	$L_{tid} = 355.2398\,m$
	Acceleration due to gravity	$g = 9.81\,\mathrm{m\,s}^{-2}$
	Buoyancy frequency	$N_b = 10^{-3}\,\mathrm{s}^{-1}$
Domain	Total length	$L = 6000\,\mathrm{km}$
	Water depth	$H = 5\,\mathrm{km}$
	Ridge amplitude	$A = 1.8\,\mathrm{km}$
	Ridge width parameter	$d = 12.5\,\mathrm{km}$
	Total time	$T_{tot} = 30\,\mathrm{days}$
Discretization	Central region length	$L_{cent} = 819.2\,\mathrm{km}$
	Number of horizontal points in the centre	$I_{cent} = 8192$
	Number of horizontal points on sides	$I_{side} = 2000$
	Number of vertical points	$J = 192$
	Cell width (central domain)	$\Delta x = 100\,\mathrm{m}$
	Cell height (deep water)	$\Delta z = 26.042\,\mathrm{m}$
	Cell height (shallow water)	$\Delta z = 16.667\,\mathrm{m}$
	Maximum time step	$\mathrm{d}t = 30\,\mathrm{s}$
Non-dimensional	Criticality parameter	$\alpha(\theta = 0°) = 1.5424$
		$\alpha(\theta = 10°) = 1.5681$
		$\alpha(\theta = 20°) = 1.6497$
		$\alpha(\theta = 30°) = 1.8040$
		$\alpha(\theta = 40°) = 2.0696$
	Tidal excursion parameter	$L_{tid}/d = 0.0284$
	Ridge aspect ratio	$d/A = 6.9444$
	Ratio of elevation and depth	$A/H = 0.36$

TABLE 1. Problem parameters.

3. Methods

3.1. *Model*

The numerical scheme used to solve (2.1) is a finite volume method based on the second-order projection technique developed by Bell, Collela & Glaz (1989) and extended to stratified flows by Bell & Marcus (1992) and to quadrilateral grids by Bell, Solomon & Szymczak (1989). The numerical scheme uses a second-order Godunov upwind scheme with a monotonized slope computation which provides selective numerical dissipation and diffusion near sharp gradients. This damps energy accumulation at small scales. The description of the model can be found in Lamb (1994).

The model uses a terrain-following grid. The total domain R is discretized with two staggered grids for the evaluation of scalar and vector unknowns: vector grid points are located at the centres of finite volumes and scalar grid points are located at the nodes of the finite volumes. Each grid can be split into three parts with respect to the horizontal resolution: the central region of length $L_{cent} = 819.2\,\mathrm{km}$ with high horizontal resolution of $\Delta x = 100\,\mathrm{m}$ and two side regions of length $L_{side} \approx 2887\,\mathrm{km}$

with lower horizontal resolution of $\Delta x = 1500$ m. The grid spacing varies smoothly from one region to another. The purpose of the side regions is to allow the fast large-scale waves generated at the centre to propagate away from the source without reflection. The length of the domain is chosen so that the waves have just enough time to reach the boundaries, but not enough time to affect the middle part after reflection.

The vector grid discretizing the central part of the domain is given by the physical coordinates $\{x_{ij}, z_{ij}\}$:

$$\left.\begin{aligned} x_{ij} &= -L_{cent}/2 + \left(i + \tfrac{1}{2}\right)\Delta x, & \Delta x &= \frac{L_{cent}}{I}, \\ z_{ij} &= -H + h(x) +_{ij} \left(j + \tfrac{1}{2}\right)\Delta z_{ij}, & \Delta z_{ij} &= \frac{H - h(x_{ij})}{J}, \end{aligned}\right\} \tag{3.1}$$

where $I = 8192$ and $J = 192$ are the number of points in the vertical and horizontal direction, respectively.

The time-stepping procedure allows a variable time step based on the Courant–Friedrichs–Lewy (CFL) condition for the upwind method. However, the maximum time step was set to a relatively small value $\mathrm{d}t = 30$ s, so the time-step did not actually change throughout the computation, except for some small intervals of time.

3.2. *Data*

Five numerical experiments that we discuss in this work are defined by the Coriolis frequencies in table 1, corresponding to latitudes $\theta = 0°, 10°, 20°, 30°$ and $40°$ North. For each experiment the model was set up to store a set of data composed of time series at 30 min intervals of the horizontal velocity u at each grid point in the central domain. Values of u are denoted by $\{u^n_{ij}\}$, where $i = 0, 1, \ldots, I-1$, $j = 0, 1, \ldots, J-1$ are the indices of the corresponding grid coordinates $\{x_{ij}, z_{ij}\}$; the superscript $n = 0, 1, \ldots, N-1$ corresponds to the temporal equipartition $t_n = (n+1)\Delta t$ covering the time period of 30 days, where the sampling interval is $\Delta t = 30$ min and the number of samples $N = 1440$. Even if the time step $\mathrm{d}t$ used by the model is not always 30 s, the model guarantees that the data are stored at the equidistributed sampling times by changing the time step appropriately just before storing the data.

In order to choose an appropriate sampling time step Δt and a reference frame, we compared spectra of the baroclinic horizontal velocity in the Lagrangian, Eulerian and barotropic-Lagrangian reference frame. Both the sampling time interval and reference frame affect the spectrum of the velocity. The sampling rate defines the amount of aliasing in the spectral estimation. The reference frame may lead to the appearance of Doppler-shifted frequencies in the spectral estimation. Ideally, working in the Lagrangian reference frame eliminates all Doppler-shifted frequencies. However, it is expensive to calculate all data sets in the Lagrangian reference frame. We found that the barotropic-Lagrangian reference frame with the sampling time interval of 30 min is an acceptable compromise for our purposes. In order to illustrate why the barotropic-Lagragian reference frame suits us, let us consider a concrete example of the spectral estimation performed for different reference frames and the case 0° N.

The first set of time series, representing the baroclinic velocity in the Eulerian reference frame, is given by $u^{tEul}(x, z, t) = u(x, z, t) - U(t)H/[H - h(x)]$ sampled in time with the sampling interval $\Delta t = 5$ min at sixteen uniformly distributed locations for $x \in [0, 40]$ km.

The second set of time series, representing the baroclinic velocity in the Lagrangian reference frame, is given by $u^{Lag}(\tilde{\xi}, \tilde{\eta}, t) = u(\tilde{\xi}, \tilde{\eta}, t) - U(t)H/[H - h(\tilde{\xi})]$ corresponding to the fluid particles whose trajectories are given by $(\tilde{\xi}(t), \tilde{\eta}(t))$ and whose initial

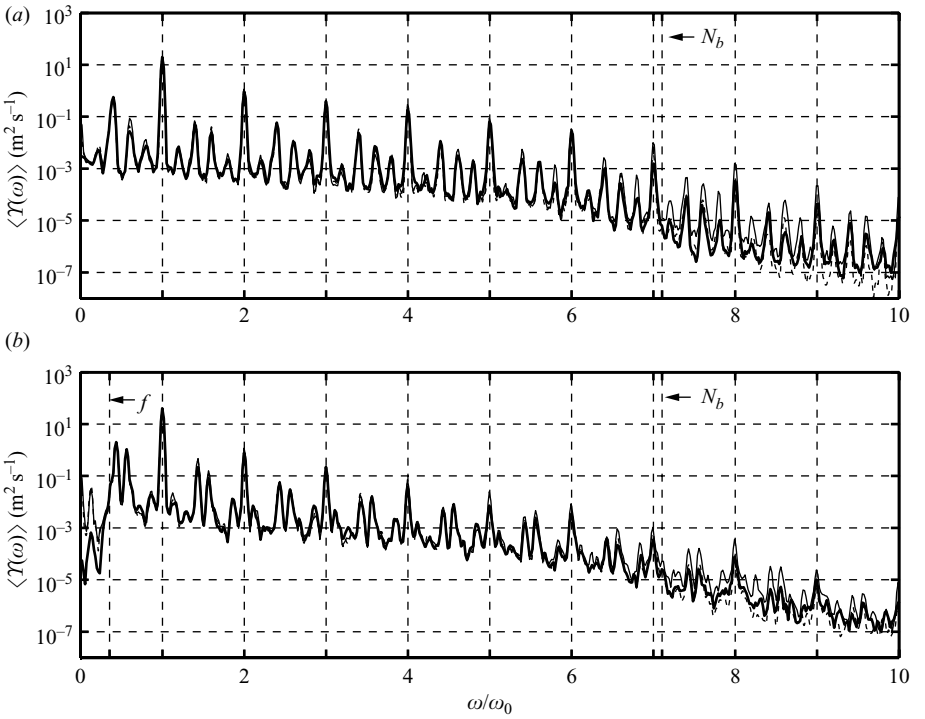

FIGURE 1. One-dimensional spectra of the horizontal velocity at latitude (*a*) 0° and (*b*) 20° N: Lagrangian reference frame (thick solid line), Eulerian reference frame (thin solid line), barotropic-Lagrangian reference frame (dashed line). The vertical dashed line to the right of $\omega/\omega_0 = 7$ indicates the buoyancy frequency.

locations are the same sixteen points as for $u^{Eul}(x, z, t)$; the time series are sampled in time with the sampling interval $\Delta t = 5$ min.

The third set of time series, representing the baroclinic velocity in the barotropic-Lagrangian reference frame, is given by $u^{bar}(\xi, \eta, t) = \tilde{u}(\xi, \eta, t) - U(t)H/[H - h(\xi)]$ such that at the initial moment, (ξ, η) coincide with the coordinates (x, z) at the same sixteen location as for $u^{Eul}(x, z, t)$; the time series are sampled in time with the larger sampling interval $\Delta t = 30$ min.

The time series start deviating after the time period of about one day; however, the difference does not grow significantly in time. The spectra $\Upsilon^{Eul}(\omega)$, $\Upsilon^{Lag}(\omega)$ and $\Upsilon^{bar}(\omega)$, corresponding to the time series $u^{Eul}(x, z, t)$, $u^{Lag}(\tilde{\xi}, \tilde{\eta}, t)$, and $u^{bar}(\xi, \eta, t)$ at different locations, were evaluated using the direct spectral estimator described in the next section. For the estimator we used a window given by the prolate spheroidal sequence of the third order. The Nyquist frequency for the sampling time interval $\Delta t = 30$ min is $\omega_{Nyq} \approx 12.4\omega_0$, six times smaller than the Nyquist frequency for the sampling interval $\Delta t = 5$ min. Figure 1(*a*) compares the spectra $\langle \Upsilon^{Eul}(\omega) \rangle$, $\langle \Upsilon^{Lag}(\omega) \rangle$ and $\langle \Upsilon^{bar}(\omega) \rangle$ for the three reference frames, where $\langle \cdot \rangle$ denotes averaging over different locations.

All the spectra are fairly close and capture the peaks at the same frequencies, consisting of harmonics and interharmonics. Thus, to define the spectral content of the flow, we could use any of the three reference frames. The decay rate of the three spectral estimations is approximately the same, indicating that the level of aliasing,

which should be more pronounced for the spectrum $\Upsilon^{bar}(\omega)$ owing to lower temporal resolution, is insignificant.

Although all of the spectra show similar energetic frequencies, the spectrum $\langle\Upsilon^{bar}(\omega)\rangle$ is closer to the spectrum $\langle\Upsilon^{Lag}(\omega)\rangle$ than is the spectrum $\langle\Upsilon^{Eul}(\omega)\rangle$. For the frequency range $\omega \in [5\omega_0, 10\omega_0]$, the spectrum $\langle\Upsilon^{Eul}(\omega)\rangle$ is larger than the other two. Thus, for the frequencies $\omega \in [0, 10\omega_0]$, the spectrum $\langle\Upsilon^{bar}(\omega)\rangle$ represents a better approximation of the spectrum $\langle\Upsilon^{Lag}(\omega)\rangle$.

Figure 1(*b*) demonstrates an analogous comparison of the spectra $\langle\Upsilon^{Eul}(\omega)\rangle$, $\langle\Upsilon^{Lag}(\omega)\rangle$ and $\langle\Upsilon^{bar}(\omega)\rangle$ for the case $\theta = 20^\circ$ N. The spectra are similar and capture the same frequencies. The main differences are observed outside the free internal wave range. For the frequencies $\omega > N_b$, the spectrum $\langle\Upsilon^{Eul}(\omega)\rangle$ is again larger than the other two. Also, the spectrum $\langle\Upsilon^{Lag}(\omega)\rangle$ corresponding to the Lagrangian reference frame has a weaker peak at the subinertial range.

In the rest of the work, we will analyse the spectrum of the horizontal velocity in the barotropic-Lagrangian reference frame.

3.3. *Spectral analysis*

To analyse energy transfers within the modelled flow, we estimate two functions: the average spectrum $\Upsilon(\omega)$ characterizing the distribution of energy in the flow with respect to different frequencies; and the spectrogram $S(\omega, t)$ representing the evolution of the spectrum with respect to time.

3.3.1. *Spectrum*

Let r be a generic function representing the horizontal baroclinic velocity $\tilde{u}$ in our simulations. We let $\boldsymbol{r}$ be the set of N values of the function r at the time moments $t_n = n\Delta t$:

$$\boldsymbol{r} = \begin{vmatrix} r_0 \\ r_1 \\ \vdots \\ r_{N-1} \end{vmatrix} \text{ with } r_n = r(t_n),\ n = 0, 1, \ldots, N-1.$$

Let $S(\omega)$ with $\omega \in [0, \infty)$ be the continuous one-sided power spectrum of the process $r(t)$, such that $S(\omega)\mathrm{d}\omega$ is the average contribution to the power from components with frequencies from the interval $[\omega, \omega + \mathrm{d}\omega]$. Total power of the process $r(t)$ on the time interval $[0, T_{tot}]$ is, then,

$$P_{tot} \equiv \frac{1}{T_{tot}} \int_0^{T_{tot}} r^2(t)\,\mathrm{d}t = \int_0^{+\infty} S(\omega)\,\mathrm{d}\omega \approx \frac{1}{T_{tot}} \sum_{n=0}^{N-1} r_n^2 \Delta t. \tag{3.2}$$

We estimate the spectrum $S(\omega)$ using a direct spectral estimator described in Percival & Walden (1993):

$$\hat{S}(\omega) = \frac{\Delta t}{\pi} \left| \sum_{n=0}^{N-1} g_n r_n \exp(-\mathrm{i}\omega t_n) \right|^2,\ \omega \in [0, \omega_{Nyq}) \tag{3.3}$$

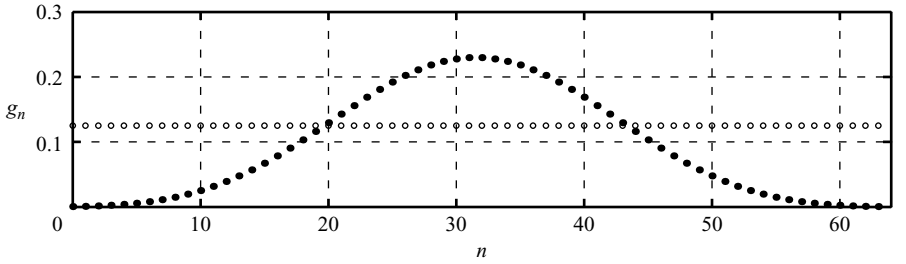

FIGURE 2. The shape of the window given by a discrete prolate spheroidal sequence used for the spectral analysis (dots) compared to the default rectangular window (circles) for $N = 64$.

where $\omega_{Nyq} = \pi/\Delta t \approx 1.75 \times 10^{-3}\,\mathrm{s}^{-1}$ is the Nyquist frequency and g_n is a data window satisfying the condition

$$\sum_{n=0}^{N-1} g_n^2 = 1. \tag{3.4}$$

The spectral estimator $\hat{S}(\omega)$ in (3.3) is defined on a continuous interval $[0, \omega_{Nyq}]$. We use (3.3) directly when we need to calculate the spectrum at a single given frequency. The evaluation of the spectral estimation $\hat{S}(\omega)$ at a large number of frequencies can be done efficiently with the use of zero-padding and the fast Fourier transform (FFT) described by Cooley & Tukey (1965). In this paper, we use 2^{13} frequencies to discretize the interval $[0, \omega_{Nyq}]$.

Figure 2 illustrates the shape of the window given by a discrete prolate spheroidal sequence of the third order that we used in this work. The window corresponds to the spectral resolution $12\pi/T_{tot} \approx 1.4544 \times 10^{-5}\,\mathrm{s}^{-1}$, i.e. each energetic frequency in the spectrum is represented by a peak with the bandwidth $12\pi/T_{tot}$. We compared several spectral estimations with different resolutions and found that with a resolution of $12\pi/T_{tot}$ the spectral estimation has no appreciable leakage in the high-frequency range of the spectrum, and, also, most of the observed energetic frequencies in the spectral estimation are well-resolved.

The variance of the spectral estimator $\hat{S}(\omega)$ can be reduced by averaging spectra for different realizations of the process $\boldsymbol{r}$. For example, let us consider the procedure of calculating the average spectrum of the flow within 40 km of the hill. For each coordinate $(\xi_{ij}^n, \eta_{ij}^n)$ in the barotropic-Lagrangian reference frame, such that $|\xi_{ij}^0| < 40\,\mathrm{km}$, we calculate the spectrum $\hat{S}_{ij}(\omega)$ of the corresponding time series $\tilde{u}_{ij}^n$. Next, we average the spectra $\hat{S}_{ij}(\omega)$ over i and j and obtain the average spectrum $\Upsilon(\omega)$:

$$\Upsilon(\omega) = \langle \hat{S}_{ij}(\omega) \rangle,$$

where the angle brackets indicate averaging over indices i and j.

3.3.2. *Spectrogram*

When the time-series $\boldsymbol{r}$ is part of a non-stationary signal, it is useful to estimate the spectrum on consecutive intervals of time in order to see how the spectrum evolves in time. In order to calculate the spectrogram, we split the sequence $\boldsymbol{r}$ into $N - M + 1$

subsequences of length M:

$$\left.\begin{array}{lcl} \boldsymbol{r}^0 & = & \{\ r_0, \quad r_1, \quad \ldots\ , r_{M-1}\ \}, \\ \boldsymbol{r}^1 & = & \{\ r_1, \quad r_2, \quad \ldots\ , r_M\ \}, \\ \cdots\cdots & & \\ \boldsymbol{r}^{N-M} & = & \{\ r_{N-M}, \quad r_{N-M+1}, \quad \ldots\ , r_{N-1}\ \}, \end{array}\right\} \tag{3.5}$$

where each sub-sequence $\boldsymbol{r}^k$ corresponds to a time interval $[t_k, t_{k+M-1}]$. For each sub-sequence $\boldsymbol{r}^k$ we calculate the spectral estimation $\hat{S}^k(\omega)$ using the estimator (3.3) with the same window. We define the spectrogram $\hat{S}(\omega, t)$ at the discrete times corresponding to the centres of the time intervals $[t_k, t_{k+M-1}]$ as follows:

$$\hat{S}\left(\omega, \frac{t_k + t_{k+M-1}}{2}\right) = \hat{S}^k(\omega). \tag{3.6}$$

The choice of the sub-sequence length is arbitrary; however, it should be short enough to capture the evolution appropriately while long enough to ensure that the significant features of the spectrum are resolved. Taking into account this trade-off, we found that the length of sub-sequence $M = N/3 = 480$ is a reasonable value, it gives the evolution of the spectrum over the time period of 20 days with a spectral resolution of $12\pi/T$, where $T = 10$ days.

Several alternative techniques could have been used to analyse the evolution of spectra. One of the most important approaches is wavelet analysis. To investigate how the energetics of different spectral components vary with time, we used, in addition to the spectrogram, the continuous wavelet transform with Gauss shape functions of different orders and obtained results nearly identical to those given by the spectrogram. For the sake of simplicity, we will demonstrate the results obtained using spectrograms in this paper.

4. Results

For the purpose of systematic analysis, our results may be considered under the following headings: (i) underlying dynamics; (ii) spectrum of the flow; (iii) spatial distribution of harmonics and interharmonics; (iv) spectrum evolution; (v) vertical scales of harmonics and interharmonics; (vi) instability description; (vii) the cause of subharmonics.

4.1. *Underlying dynamics*

The solution to (2.1) consists of progressive and forced (trapped) internal waves, whose dominant frequencies, according to the spectrum of the flow, form a discrete set of tidal harmonics and interharmonics. Both progressive and forced waves can be seen in figure 3, which shows snapshots of the horizontal velocity field within 40 km of the ridge at time $t = 30$ days for the five latitudes. Vertical profiles of the horizontal velocity at $x = 13$ km are shown to the right-hand side of each contour plot. These illustrate the strength of the flow in the tidal beams. The progressive and trapped waves are generated where the flow is highly nonlinear: the region near the ridge and regions where strong progressive internal waves collide or reflect from the boundary. Only the strongest waves are seen in the velocity snapshots.

Some internal waves in the internal wave field overturn and break. The overall wave field, however, is mostly immune to the shear instabilities and no overturning happens away from strongly nonlinear regions. For all times, the Richardson number $Ri = N_b^2/(\partial u/\partial z)^2$ is less than 0.25 only within small regions where strong nonlinear

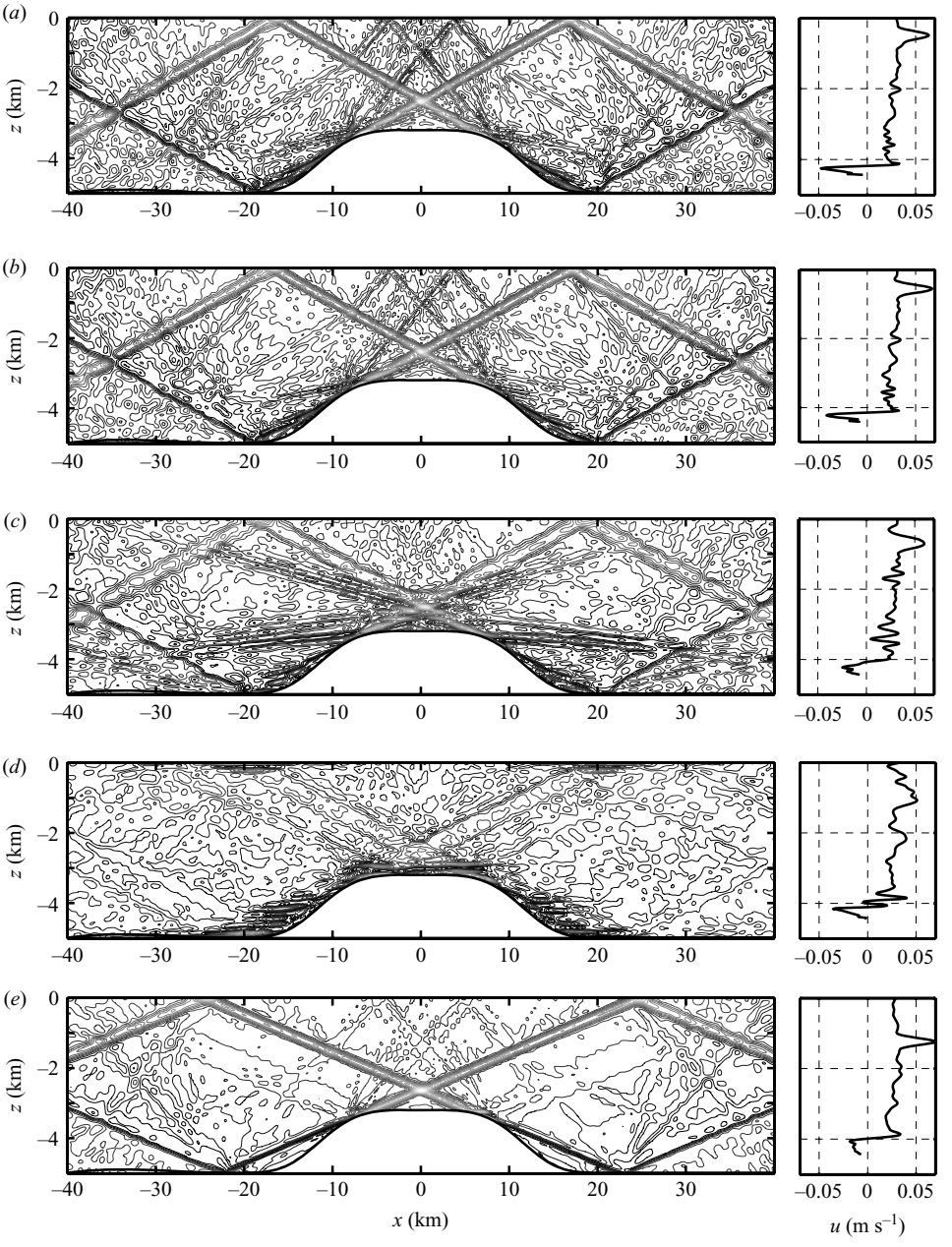

FIGURE 3. Contours of the horizontal velocity field at different latitudes at $t = 30$ days (*a*) $\theta = 0°$N, (*b*) 10°N, (*c*) 20°N, (*d*) 30°N, (*e*) 40°N. The right-hand panels show horizontal velocity profiles at $x = 13$ km.

dynamics take place. Typically, this corresponds to the breaking of waves shoaling onto the top of the ridge, similar to the breaking of surface waves shoaling onto the shore. However, for the case 30° N, some overturning happens to the trapped waves in the vicinity of strongly nonlinear regions where the tidal beams hit the bottom or surface.

Progressive waves have frequencies within the range (f, N_b). Since N_b is constant, waves of a single frequency ω can form a straight beam, whose slope r is determined by the three frequencies ω, N_b and f and is given by (1.1). As the topography is supercritical, strong waves of tidal frequency generated at the edges of the ridge, where the slope is critical, propagate both upward and downward, so that pronounced tidal beams are seen above the top and along the side of the ridge. The second harmonic $2\omega_0$ and other higher harmonics have slopes steeper than any part of the ridge, so their corresponding beams emanating from the generation sites at the edges of the ridge, are directed upward only. For most cases, progressive waves dominate the flow, which is manifested in the pronounced beam structure (figure 3*a–c*, *e*).

Trapped waves have frequencies outside (f, N_b) and some of them are seen as horizontally elongated patches near the generation sites. For example, when $\theta = 30^\circ$ N, we observe strong waves of subtidal frequency $\omega \approx 0.5\omega_0 < f$ that do not propagate away, but are trapped near the ridge and near the regions where the tidal beams hit the surface (see figure 3*d*).

The spectra of the internal waves (figures 5 and 6) that will be explained in the next section, have a discrete set of dominant frequencies, either tidal harmonics or interharmonics; here, we consider how tidal harmonics and interharmonics appear in the velocity field. The major part of the energy in the flow is concentrated in tidal harmonics, i.e. waves corresponding to the multiples of the tidal frequency: $\omega = n\omega_0$ where $n \in \mathbb{N}$, except at 20° and 30° N where the strong subharmonic spectral peak is greater in magnitude than the peak at frequency $2\omega_0$. Some of the beams corresponding to the strongest harmonics are seen in figure 3, e.g. the first and second harmonics are seen to be the dominant features of the velocity field for the cases $\theta = 0^\circ$ and 10° N. Tidal harmonics with $n < N_b/\omega_0$ are progressive waves that contribute to the far field away from the generation site, and tidal harmonics with $n \geqslant N_b/\omega_0$ are trapped near the generation site. At the early stage of the flow development, tidal harmonics are generated through tide–topography interaction near the edges of the ridge. At this stage, the solution is similar to the analytical one obtained by Bell (1975). Bell considered a similar problem in a non-rotating fluid of infinite depth, and approximated the operator $\boldsymbol{u} \cdot \nabla$ in the governing equations with $U(t)\partial/\partial x$, i.e. only advection by the horizontal component of the barotropic tide plays a role. Bell's solution was later extended to the case of finite depth by Khatiwala (2003). The solutions obtained by Bell and Khatiwala are given by linear superpositions of tidal harmonics emanating from near the ridge; as in our simulations, the energy in harmonics $n\omega_0$ decays rapidly with n.

The progressive tidal beam harmonics produced by tide–topography interaction propagate away from the ridge and eventually either intersect with other waves or reflect from a boundary. In any of these events, the incident wave interacts nonlinearly with the encountered or the reflected wave, and, as a result, may produce waves at the combination frequencies, which are also from the set of tidal harmonics $n\omega_0$ with $n \in \mathbb{N}$. For example, if a wave of frequency $2\omega_0$ interacts with itself after reflection, it produces a wave of frequency $4\omega_0$, then the generated wave interacts with the initial wave producing a wave of frequency $6\omega_0$, and so on. The interaction and the energetics of colliding and reflecting internal wave beams in a non-rotating fluid was described analytically by Tabaei *et al.* (2005). They assumed that the flow away from the generation sites was weakly nonlinear and sought the solution as a composition of tidal harmonics. If the flow was indeed weakly nonlinear, the internal wave field within a finite distance of the ridge would eventually resolve into a quasi-steady beam structure. However, the flow consisting of tidal harmonics is far from reaching

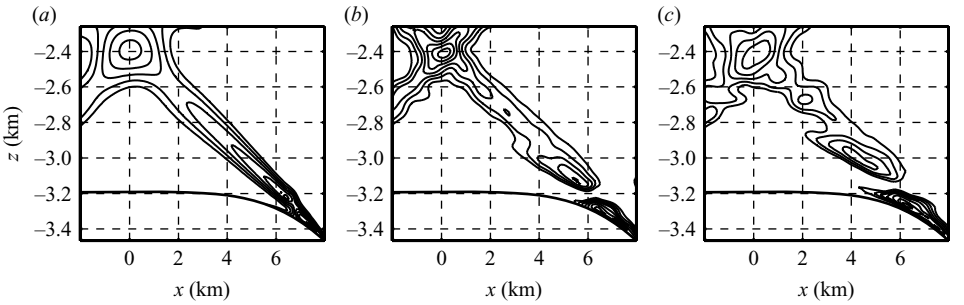

FIGURE 4. The tidal beam undergoing instability for the case $\theta = 20^\circ$ N, given by the contours $|u| = \{0.05, 0.06, \ldots, 0.13\}\,\mathrm{m\,s^{-1}}$ at (*a*) $t = 2.5T_0$, (*b*) $7.5T_0$, (*c*) $12.5T_0$. $T_0 = 12.4$ h is the tidal period.

an equilibrium: the strong beams of tidal frequency are perturbed periodically by the topography and other beams, and soon become unstable (see figure 4 for an illustration). Instabilities of, possibly, the same nature have been observed in the ocean (Martin & Rudnick 2007). In our simulations, as a result of instabilities, waves of interharmonic frequencies are generated.

Among all interharmonics generated in the flow and seen in the spectra (figures 5 and 6), the most evident are subharmonics, i.e. interharmonics of subtidal frequency $\omega < \omega_0$ (e.g. figure 3*a–c*). Beams of subharmonic frequencies are less steep than any of the beams with frequency $n\omega_0$, so subharmonics are easily detected in a velocity field. For example, in case of $\theta = 20^\circ$ N, four strong beams of subtidal frequencies (determined by the slope) emanate from the two destabilized beams of tidal frequency above the top of the ridge (figure 3*c*). Similar beams of subharmonic frequencies, although less pronounced, can be seen for the cases $\theta = 0^\circ$ and 10° N (figure 3*a*, *b*). Closer inspection of the velocity fields reveals that the tidal beams become unstable and generate subharmonics not only above the ridge, but also on its sides and where the tidal beams are reflected from the top and the bottom of the domain.

Apart from subharmonics, the flow has other interharmonics whose frequencies are larger than the tidal frequency. Their presence can be explained from the following simple reasoning: any subharmonic ω_α interacting with harmonics $n\omega_0$, can produce waves of frequency $n\omega_0 + \omega_\alpha$, $n \in \mathbb{N}$. If the energy of a subharmonic is comparable to that of the dominant harmonic ω_0, then the energetics of higher interharmonics should be comparable to those of higher harmonics $n\omega_0$ with $n \geqslant 2$. In general, the generation of a wave at frequency $\omega_\alpha \in [0, \omega_0)$ should be accompanied by the generation of waves at frequencies $\omega_\alpha + n\omega_0$ with $n \in \mathbb{N}$. The higher interharmonics are harder to detect directly in a velocity field, not only because they are weaker, but, also, because their slopes can be easily mistaken for those of tidal harmonics. Their presence becomes obvious after considering the average spectra of the flow and spatial distributions of waves with interharmonic frequencies.

4.2. *Spectrum of the flow*

In order to quantify the distribution of energy among different harmonics and interharmonics we estimated the average spectra of the flow in different regions for the different latitudes. The spectra reveal the most important spectral components of the flow and quantify their energetics.

Figure 5 shows the average spectra of the flow within 40 km of the ridge for the five cases. The spectra are calculated from the horizontal velocity time series in the

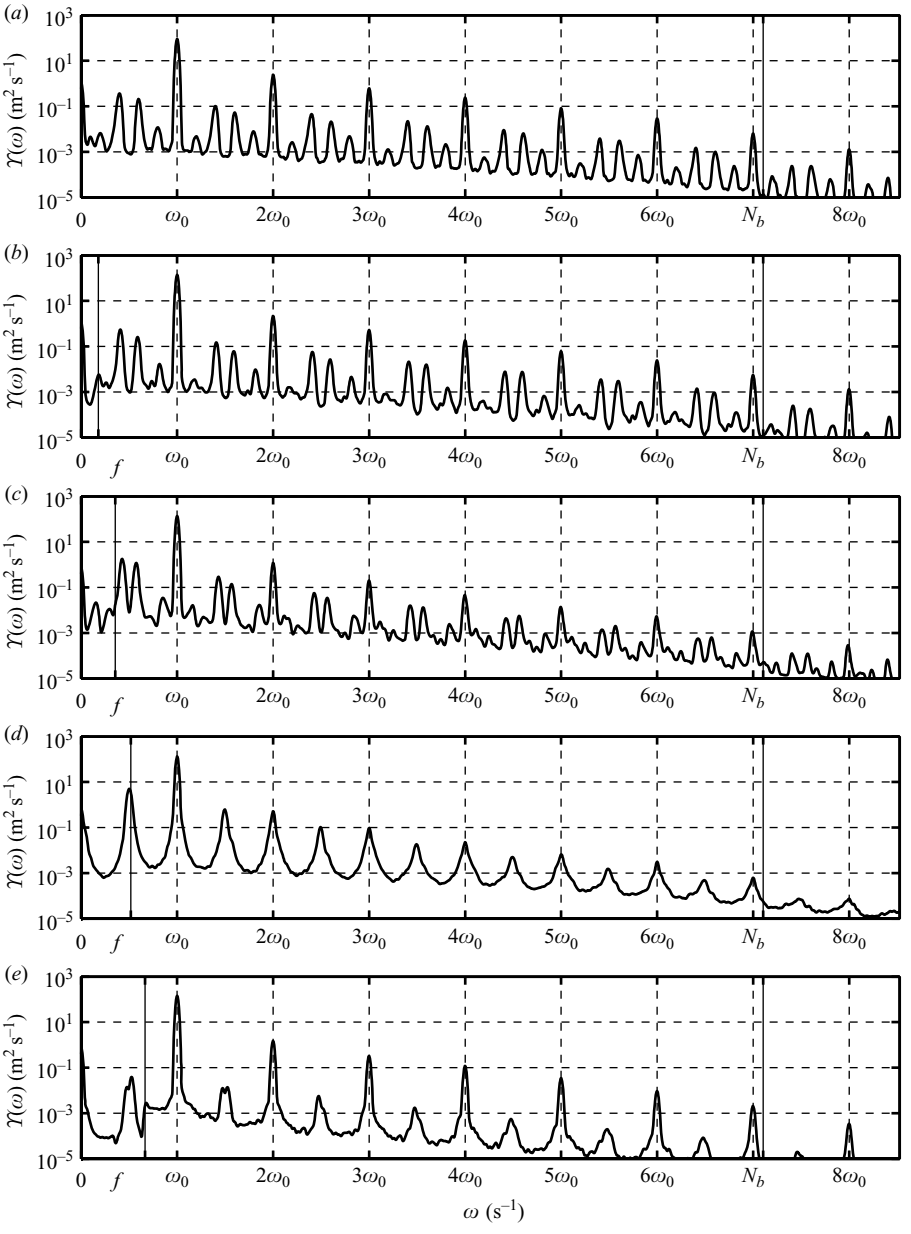

FIGURE 5. One-dimensional spectrum of the flow within 40 km of the ridge for the five cases (*a*) 0°N, (*b*) 10°N, (*c*) 20°N, (*d*) 30°N, (*e*) 40°N.

barotropic-Lagrangian reference frame. The spectra have a self-similar structure with prominent peaks at a discrete set of tidal harmonics and interharmonics.

The spectra are self-similar in the following sense: the shape of each spectrum in the low-frequency range $(0, \omega_0]$ nearly copies itself in the further frequency ranges $(n\omega_0, (n+1)\omega_0]$ for $n \in \mathbb{N}$. As there are only a few dominant frequencies in the interval $(0, \omega_0]$, the spectrum is comprised of peaks at the tidal harmonics $\{n\omega_0\}$ and the interharmonics $\{\omega_\alpha + n\omega_0\}$, where $n \in \mathbb{N}$ and ω_α can be any of the subharmonics.

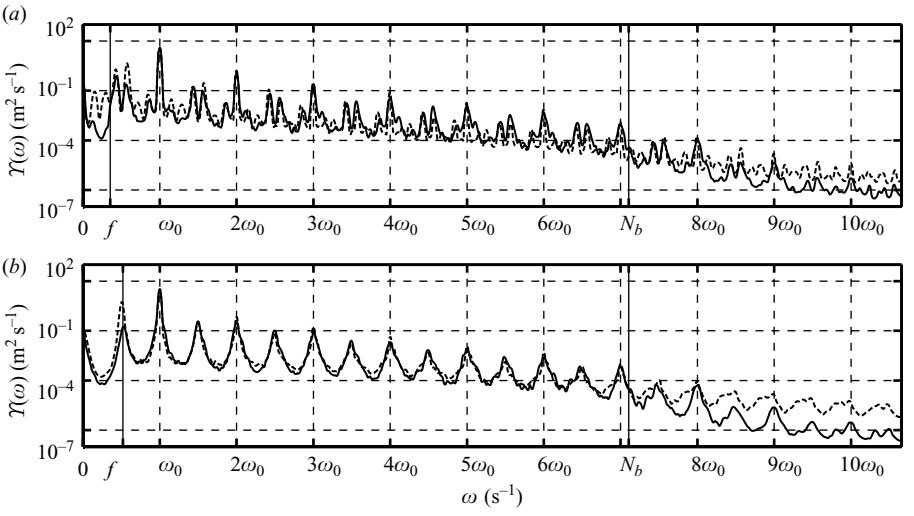

FIGURE 6. One-dimensional spectra of the flow for the cases (*a*) $\theta = 20°$, (*b*) 30° N: $-5 \leqslant x \leqslant 5$ km (dashed line), $30 \leqslant x \leqslant 40$ km (solid line).

For the spectra shown in figure 5, both harmonics $\{n\omega_0\}$ and interharmonics $\{\omega_\alpha + n\omega_0\}$ decay with n at a similar exponential rate.

One of the consequences of the observed self-similarity and exponential rate of decay is that if a subharmonic ω_α has less energy than the tidal frequency ω_0, then the higher interharmonics $\{\omega_\alpha + n\omega_0\}$ are also weaker than the corresponding harmonics $\{(n+1)\omega_0\}$, where $n \in \mathbb{N}$. If, on the other hand, the subharmonics are stronger than the tidal frequency, as in the case of tidal-to-subtidal conversion of motion happening, for example, in the vicinity of the ridge for the case $\theta = 30°$ N (discussed in more detail later), then the higher interharmonics can also dominate higher harmonics.

The spectral peaks at frequencies within the range (f, N_b) correspond to progressive waves; the peaks outside the range (f, N_b), to trapped waves. As the trapped waves have amplitudes comparable to those of progressive waves, the shapes of the average spectra do not allow us to distinguish trapped waves from progressive. To see which waves are trapped near the ridge (the strongest generation site) and do not propagate away, we compare the average spectra of the region $-5 \leqslant x \leqslant 5$ km on top of the ridge and the average spectra of the region $30 \leqslant x \leqslant 40$ km away from the ridge. Figure 6 demonstrates the comparison for the two latitudes $\theta = 20°$ and 30°. For the case $\theta = 20°$ N, it is seen that the peaks at frequencies less than the Coriolis frequency are virtually absent in the spectrum for the region away from the ridge, as these subinertial waves are trapped and do not reach the far-field region. For the higher frequencies $\omega > N_b$, the spectrum of the flow away from the ridge has a significantly higher drop-off rate than that of the spectrum near the ridge, which is seen for both latitudes.

The important result that can be extracted from the spectra is the existence of strong interharmonics for latitudes $\theta \leqslant 30°$ N. For the case $\theta = 40°$ N, the interharmonics are very weak, but are present. From our estimates, it follows that subharmonics, which have been observed before in spectra of internal waves (Gerkema *et al.* 2006; MacKinnon & Winters 2007), happen to be just the strongest among other interharmonics. Consistent with the aforementioned studies, the interharmonics are particularly intense at near-critical latitudes, where the critical latitude ($\theta_{cr} = 28.82°$ N)

is the latitude at which the Coriolis frequency is half the tidal frequencies. For example, at the latitude 20° N, we see that the frequencies $\omega \approx 0.4269\omega_0$ and $\omega \approx 0.5752\omega_0$ are the second and third strongest frequencies in the spectrum after the tidal frequency ω_0. However, efficient energy transfers from the tidal frequency into the subtidal range are possible for latitudes $\theta > \theta_{cr}$, when the subharmonic receiving energy is outside the range of freely propagating waves. In case $\theta = 30° > \theta_{cr}$, we observe large transfers of energy into the subtidal range, and, as can be inferred from the velocity snapshots and from the average spectrum, the frequency of at least one of the recipient subharmonic waves is a trapped subinertial wave. Thus, in this case, the generated subharmonics are not a result of a resonant triad interaction.

4.3. *Spatial distribution of harmonics and interharmonics*

Generated at various regions, propagating at numerous angles and exchanging energy, harmonics and interharmonics have a complex spatial distribution. The power spectra calculated for each spatial point indicate where a wave of a certain frequency is more or less energetic; thus, we can construct their spatial distribution. After examining spatial distributions of tidal harmonics and interharmonics at different latitudes, we found the following.

(*a*) The wave of a harmonic or an interharmonic frequency within the range (f, N_b) forms a beam whose slope is consistent with the linear dispersion relation (1.1).

(*b*) The wave of a harmonic or an interharmonic frequency outside the range (f, N_b) forms a patch near the source.

(*c*) The generation sites of a tidal harmonic include: the region near the edge of the ridge; a region where two harmonics collide; a region where a harmonic reflects from the boundary.

(*d*) The generation sites of an interharmonic include: the regions where the beam of tidal frequency becomes unstable, i.e. above the ridge, on the side of the ridge, or where the tidal beam is reflected from the boundary; the regions where an interharmonic collides with another wave.

Figures 7, 8 and 9 illustrate those points for a subset of tidal harmonics and interharmonics at latitudes $\theta = 0°$, 20° and 30° N. For a particular frequency ω_α, we calculate the matrix $\hat{S}_{ij}(\omega_\alpha)$ for the time-series $\{\tilde{u}^n_{ij}\}$. After sorting the matrix $\hat{S}_{ij}(\omega_\alpha)$, we choose approximately 32 % of $\hat{S}_{ij}(\omega_\alpha)$ with the largest values and visualize those at the corresponding coordinates (x_{ij}, z_{ij}). The 5 % of the matrix $\hat{S}_{ij}(\omega_\alpha)$ with the largest values are emphasized with a cross-hatched pattern.

For the case $\theta = 0°$, figure 7 demonstrates the distribution of the subharmonic $\omega = 0.4\omega_0$, the tidal harmonic ω_0, the interharmonic $1.4\omega_0$ and the second harmonic $2\omega_0$. The subharmonic $\omega = 0.4\omega_0$ corresponds to the strongest subharmonic peak in figure 5(*a*). The tidal harmonic has most of its energy in tidal beams generated near the edges of the ridge. The second harmonic is manifested in several beams, some of which are generated near the edges of the ridge, some, where a tidal beam hits the boundary, and some, where tidal beams intersect. The subharmonic $0.4\omega_0$ is comprised of two beams, one of which originates from the unstable tidal beam above the ridge, and another, from the unstable tidal beam on the side of the ridge. The beams corresponding to the subharmonics are wider than those of harmonics. This is because the instability initially develops at the base of the beam close to the topography and subsequently spreads further and further along the beam, i.e. the beam becomes unstable further up. Accordingly, the subharmonics generated by instabilities do not propagate from a localized source, but propagate from a considerable length of the tidal beam (see also figure 4). For the same reason, the beams of the interharmonic

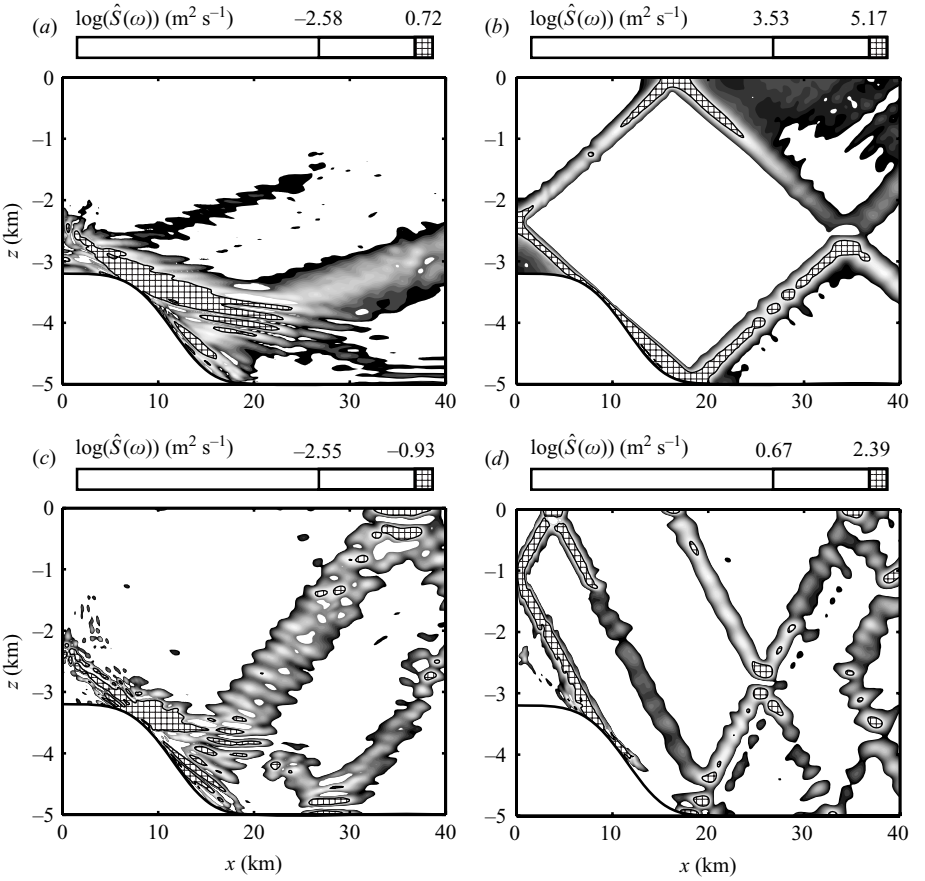

FIGURE 7. Spatial distribution of waves with different frequencies within 40 km of the ridge for the case $\theta = 0°$ N: (*a*) $\omega = 0.4\omega_0$, (*b*) $\omega = \omega_0$, (*c*) $\omega = 1.4\omega_0$, (*d*) $\omega = 2\omega_0$.

$1.4\omega_0$ are also wide. The beams corresponding to the interharmonic $1.4\omega_0$ are also seen to be generated in the regions of instability of the tidal beam (figure 7*c*).

For the case $\theta = 20°$ N, figure 8 demonstrates the two strong subharmonics $0.4269\omega_0$ and $0.5752\omega_0$ that appear in the velocity field (figure 3*c*) and in the spectra (figure 5*c*). Also shown are the corresponding interharmonics $1.4269\omega_0$ and $1.5752\omega_0$. The subharmonics are generated at three common generation sites, where the strong tidal beam, tangent to the topography, becomes unstable: above the ridge, on the side of the ridge and where the tidal beam reflects from the bottom. The beam of subharmonic frequency formed where the tidal beam reflects from the bottom is more clearly seen in the velocity field snapshot (figure 3*c*). All the interharmonics shown form beams. In particular, it is seen that the familiar 'fan' of beams emanating from the edge of the ridge consists not only of harmonics, as in Bell's solution, but, also, of interharmonics in between. The weaker interharmonics, e.g. $0.1544\omega_0$ and $0.8504\omega_0$, are not shown here because they are more susceptible to error and have a noisy spatial distribution, which is hard to interpret. It is certain, however, that they exist at the regions of instability.

For the case $\theta = 30°$ N, figure 9 demonstrates the distribution of energy corresponding to the frequency $0.5\omega_0$, ω_0, $1.5\omega_0$ and $2\omega_0$. The peak at the frequency

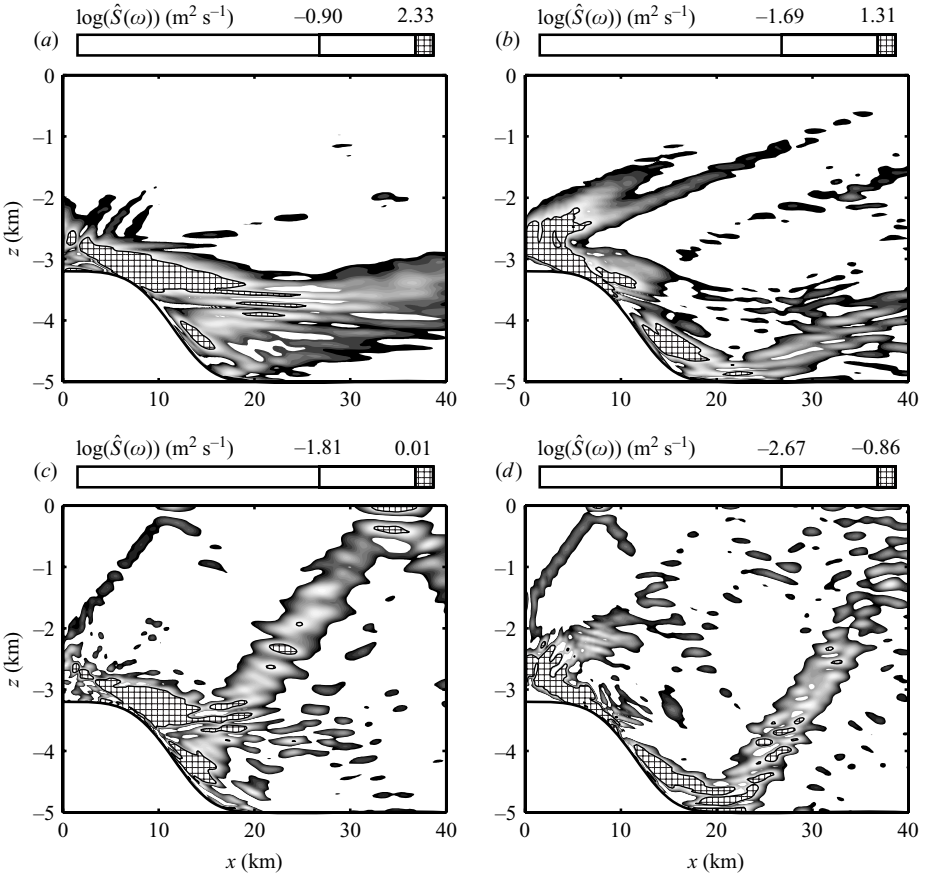

FIGURE 8. Spatial distribution of waves with different frequencies within 40 km of the ridge for the case $\theta = 20^\circ$ N: (*a*) $\omega = 0.4269\omega_0$, (*b*) $\omega = 0.5752\omega_0$, (*c*) $\omega = 1.4269\omega_0$, (*d*) $\omega = 1.5752\omega_0$.

$0.5\omega_0$ seen in figure 5 most probably corresponds to two subharmonics close to the Coriolis frequency f. The spectral resolution renders the two subharmonics almost indistinguishable. One of the subharmonics is progressive and the other is trapped. This can be deduced, in part, from figure 6, $\theta = 30^\circ$ N. The subharmonic peak corresponding to $-5 \leqslant x \leqslant 5$ km has its maximum at a frequency slightly less than the Coriolis frequency, while the weaker subharmonic peak corresponding to $30 \leqslant x \leqslant 40$ N has its maximum at a frequency slightly larger than the Coriolis frequency. Accordingly, figure 9(*a*) shows that the distribution of energy at frequency $0.5\omega_0$ has some non-zero slopes that can be attributed to the progressive wave; however, mostly, energy is concentrated near the ridge, which is the manifestation of the trapped wave. The energetic patches corresponding to the trapped subharmonic are gathered around the regions of instability of the tidal beam: above and on the side of the ridge, and where the tidal beam is reflected from the boundary. The energetic interharmonic close to $1.5\omega_0$, generated at the same generation sites as the trapped subharmonic, forms a beam whose slope is given by the linear dispersion relation. The harmonics behave similarly to the case $\theta = 0^\circ$ N.

The beam structure of the flow emerges here even more clearly than in the velocity snapshots. It is seen that the waves with subharmonic frequencies also form internal

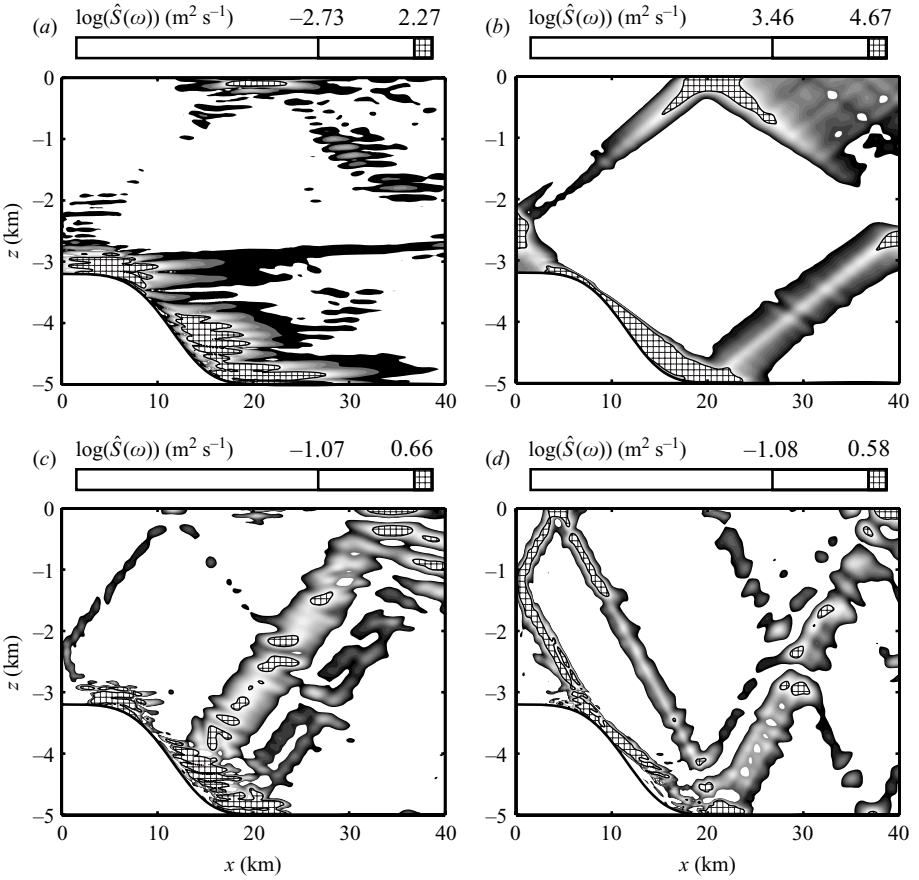

FIGURE 9. Spatial distribution of waves with different frequencies within 40 km of the ridge for the case $\theta = 30^\circ$ N: (*a*) $\omega = 0.5\omega_0$, (*b*) $\omega = 1.0\omega_0$, (*c*) $\omega = 1.5\omega_0$, (*d*) $\omega = 2.0\omega_0$.

wave beams if the frequency is within the range (f, N_b), (see, for example, figure 7*a*). The slopes of the interharmonic beams agree with the linear dispersion relation (1.1). If the interharmonic is outside the range of freely propagating waves, the wave is trapped, as in the case of the trapped subharmonic at $\theta = 30^\circ$ N.

4.4. *Spectrum evolution*

Further insight into the nature of harmonics and interharmonics can be gained by quantifying the evolution of their energetics. To do this, we calculate the spectrograms, described in § 3, that provide the evolution of the short-term spectra. The spectrograms lack intricate details of the spectrum variation, but they show the overall trends. In this section, we consider spectrograms calculated for the time periods $[t_0 - 5, t_0 + 5]$ days, where $t_0 \in [5, 25]$ days.

As a frequency is gaining or losing energy, the corresponding peak of the spectrum is either growing or decaying. Figure 10 illustrates the spectra for the cases 0° and 30° N calculated at an early time interval [0, 10] days and at a later time interval [10, 20] days. It is seen that, with time, the interharmonics gain energy, whereas the harmonics either stay unchanged or lose energy. In a similar fashion, we can analyse the energetics of each harmonic and interharmonic.

The time variation of a given harmonic or interharmonic changes smoothly with latitude. For example, figure 11 compares the evolution of the energy in the first

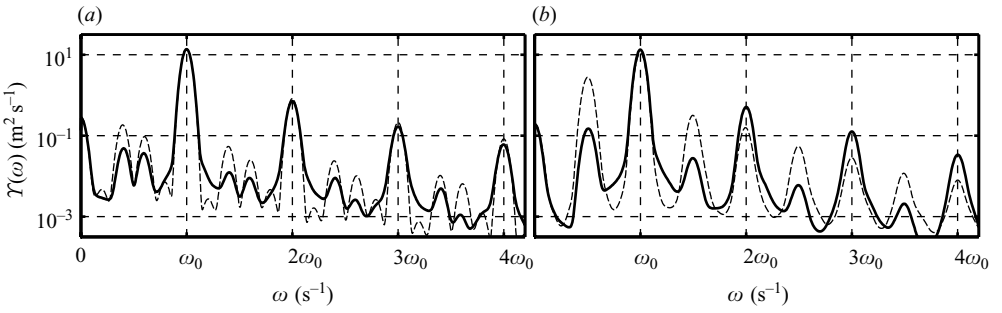

FIGURE 10. Fragments of spectra calculated for two time periods: [0, 10] days (solid line); [10, 20] days (dashed line). (*a*) 0°N, (*b*) 30°N.

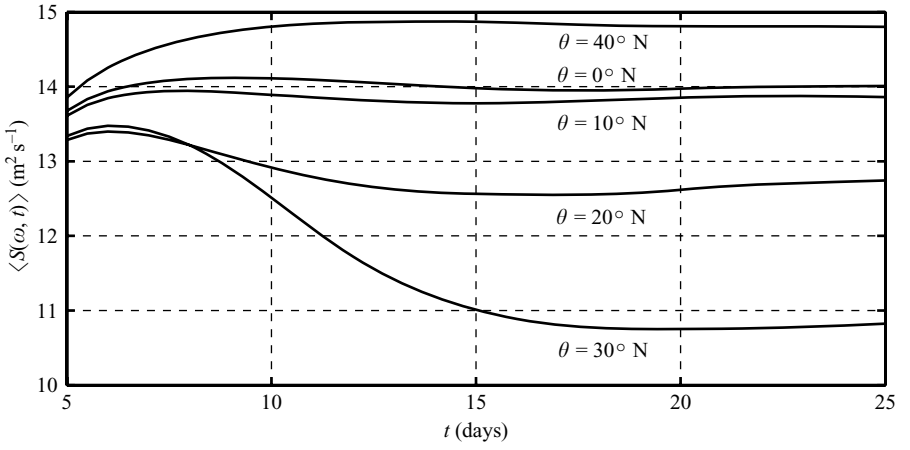

FIGURE 11. Energy of the tidal harmonic at different latitudes.

tidal harmonic at the different latitudes. The critical latitude is the case where the most efficient harmonic-to-interharmonic energy transfers take place: according to the spectrogram for the case 30° N, the energy at the tidal frequency decreases by about 20 % from its value at 5 days before reaching a steady state.

Let us consider several first harmonics and interharmonics for the two latitudes, 0° N and 30° N (figures 12 and 13). At $\theta = 0°$, the energy in the first and second harmonics grow by a small amount for about 5 days (note that the spectrogram begins at $t = 5$ days so initial growth is lost), and then they behave in a manner similar to what could be the beginning of relaxation to a steady state. The supposition that the energy in harmonics approaches a steady state is supported by the more obvious stabilization observed in the case $\theta = 30°$ N and the fact that spectrograms vary smoothly from latitude to latitude. The interharmonics seem to have a similar pattern of relaxation, but on longer time scales.

For the latitude $\theta = 30°$ N, the energy at the tidal harmonic decreases significantly (by ≈ 20 %) to a steady state within approximately 10 days. During the same 10 days, the interharmonics efficiently gain energy. It is not seen that the interharmonics have stabilized by the end of the run to a particular level.

Similar evolution of energy in the tidal and subtidal frequency was calculated by MacKinnon & Winters (2003).

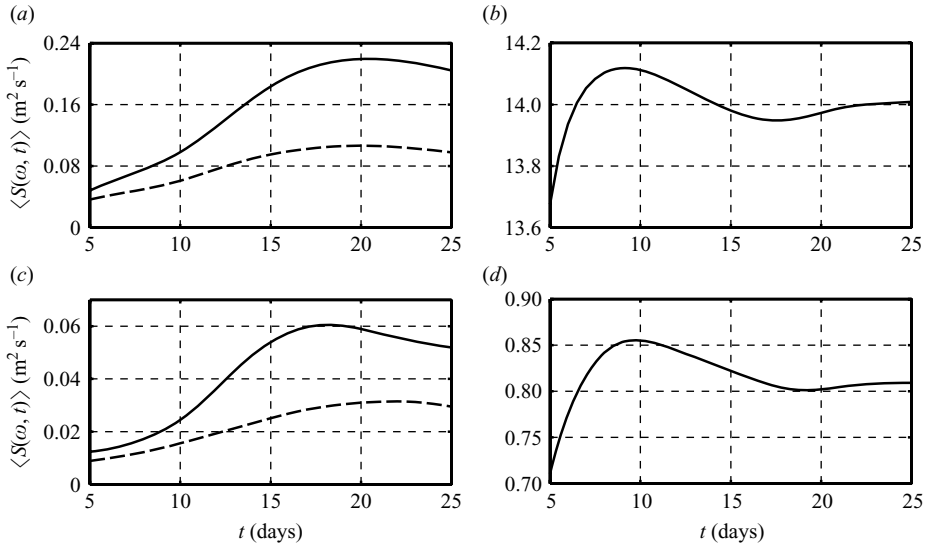

FIGURE 12. The averaged spectrogram for the flow within 40 km from the ridge at the latitude $\theta = 0°$ N: (*a*) $\omega = 0.4\omega_0$ (solid line), $\omega = 0.6\omega_0$ (dashed line), (*b*) $\omega = 1.0\omega_0$, (*c*) $\omega = 1.4\omega_0$ (solid line), $\omega = 1.6\omega_0$ (dashed line), (*d*) $\omega = 2.0\omega_0$.

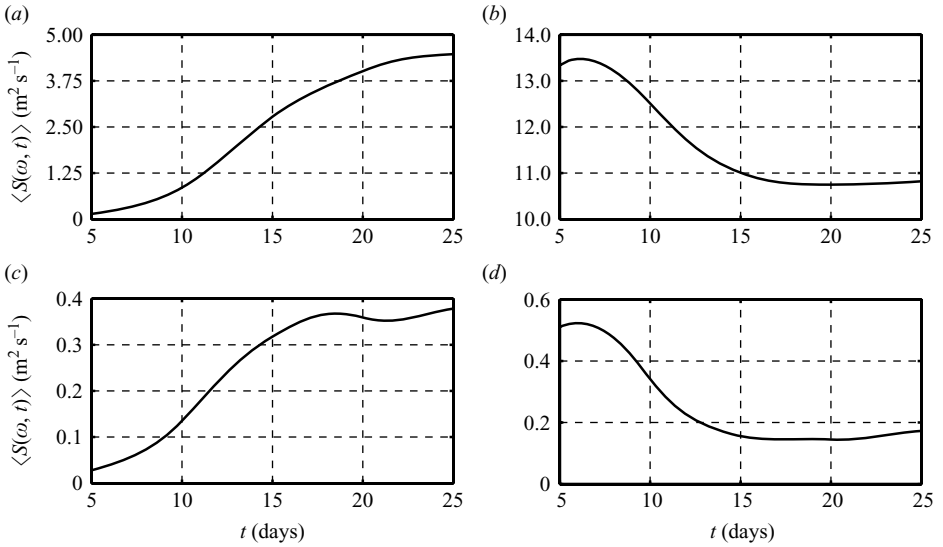

FIGURE 13. The averaged spectrogram for the flow within 40 km from the ridge at the latitude $\theta = 30°$ N: (*a*) $\omega = 0.5\omega_0$, (*b*) $\omega = 1.0\omega_0$, (*c*) $\omega = 1.5\omega_0$, (*d*) $\omega = 2.0\omega_0$.

4.5. *Vertical scales of harmonics and interharmonics*

In our runs, interharmonics have vertical scales typically smaller than those of harmonics and, thus, interharmonics should potentially be more susceptible to mixing. To compare the vertical scales of harmonics and interharmonics, we consider the velocity field in the region $20 \leqslant x \leqslant 40$ km, where the depth is constant. To capture the vertical scales that dominate the velocity field, we perform the discrete cosine transform of the array $\tilde{u}_{ij}^n$ with respect to the index j, corresponding to the vertical

coordinate:

$$\mathsf{DCT}\{\tilde{u}\}(x_i, m_l, t_n) = \beta(l) \sum_{j=0}^{J-1} \tilde{u}_{ij}^n \cos[(z_j + H)m_l], \quad l = 0, 1, \ldots, J-1, \tag{4.1}$$

where $m_l = \pi l / H$ and

$$\beta(l) = \begin{cases} \sqrt{1/J}, & l = 0; \\ \sqrt{2/J}, & l = 1, 2, \ldots, J-1. \end{cases} \tag{4.2}$$

Next, to capture temporal scales, we estimate the power spectral density of each time series $\mathsf{DCT}\{\tilde{u}\}(x_i, m_l, t_n)$ with a fixed vertical wavenumber m_l and horizontal coordinate x_i, using the same spectral estimator as in (3.3):

$$E(x_i, m_l, \omega) = \frac{\Delta t}{\pi} \left| \sum_{n=0}^{N-1} g_n [\mathsf{DCT}\{\tilde{u}\}(x_i, m_l, t_n)] \exp(-\mathrm{i}\omega t_n) \right|^2. \tag{4.3}$$

Finally, averaging over x_i spanning the interval $[20, 40]$ km, we obtain a two-dimensional spectrum $\bar{E}(\omega, m_l)$, characterizing average energy distribution with respect to the frequency ω and vertical wavenumber m_l. Average power of the baroclinic horizontal velocity is related to the spectrum $\bar{E}(\omega, m_l)$ as follows:

$$\left\langle \frac{1}{T_{tot}} \int_0^{T_{tot}} |\tilde{u}(\xi, \eta, t)|^2 \, \mathrm{d}t \right\rangle_{(\xi,\eta)} \approx \frac{1}{J} \sum_{l=0}^{J-1} \int_0^{\omega_{Nyq}} \bar{E}(\omega, m_l) \, \mathrm{d}\omega, \tag{4.4}$$

where the averaging on the left-hand side is performed over (ξ, η) such that $\xi(0) \in [20, 40]$ km.

Figure 14 shows the spectrum $\bar{E}(\omega, m_l)$ for different latitudes. The vertical scales of harmonics are dominated by low vertical modes: as the mode number increases, the energy rapidly decays. The vertical scales of interharmonics are dominated by vertical wavenumbers consistently higher than those of the corresponding harmonics. This feature was observed for subharmonics in similar spectra by MacKinnon & Winters (2003, 2007). Among all interharmonics, subharmonics have the highest vertical wavenumbers. In the case $\theta = 30^\circ$ N, subharmonics have the highest vertical wavenumbers in comparison with other latitudes.

For the cases 10°, 20° and 40°, the subinertial regions $\omega < f$ in the spectra $\bar{E}(\omega, m_l)$ are much less energetic in comparison with other regions. However, for the case $\theta = 30^\circ$ there is clearly a subinertial peak at $\omega_0/2$. Note, that the energetic patches associated with the interharmonics in figure 14 do not necessarily imply a continuous distribution with respect to the vertical wavenumber: the broad range of vertical scales with small energy values is due to leakage and the energetic patches, in fact, may be comprised of only a few waves with constant vertical wavenumbers.

4.6. *Instability description*

To illustrate how instability generates a wave with a subharmonic frequency, we consider an example of a local flow conversion from tidal frequency to a subharmonic one.

We choose the case of $\theta = 30^\circ$ N as the instability processes are particularly distinctive there and the energy transfers from the tidal frequency to the subharmonics are strong. From the spatial distribution of waves with different frequencies in figure 9, we see that the flow has strong waves of the subharmonic frequency

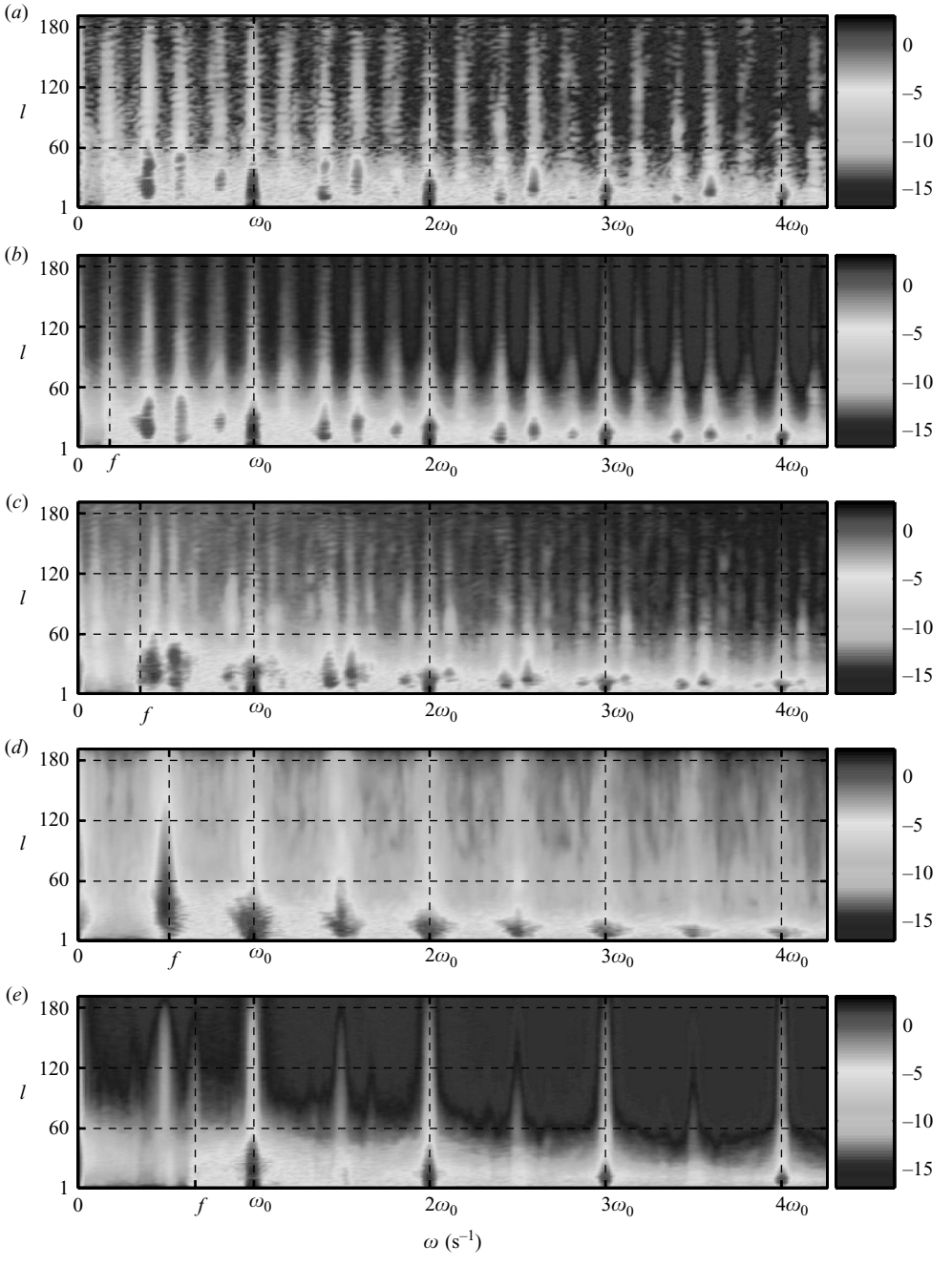

FIGURE 14. Two-dimensional spectra $\bar{E}(\omega, m_l)$ ($\mathrm{m^2\,s^{-1}}$) on the logarithmic scale calculated for $x \in [20, 40]$ km. (*a*) $\theta = 0°$, (*b*) 10°N, (*c*) 20°N, (*d*) 30°N, (*e*) 40°N.

near the top of the ridge and along the side. Let us consider the particular location $(x, z) = (15.7, -4.321)$ km. There, according to the local velocity spectrum, the subharmonic frequency is particularly strong. Figure 15(*a*) shows the velocity time series in the barotropic-Lagrangian reference frame corresponding to this location.

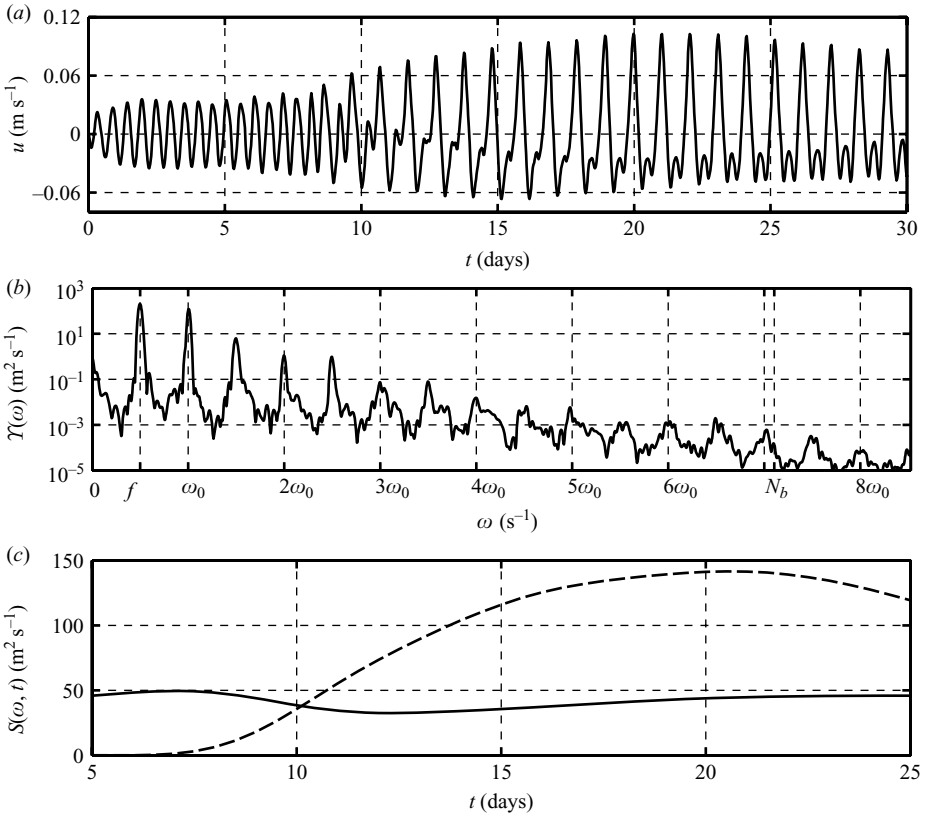

FIGURE 15. Development of instability at $\theta = 30^\circ$ N near the location $x = 15.7$ km and $z = -4.321$ km: (*a*) the time-series of the horizontal velocity in the barotropic-Lagrangian reference frame, (*b*) averaged spectrum over 30 days, (*c*) spectrogram of the tidal frequency (solid line) and frequency $0.5\omega_0$ (dashed line).

The tidal frequency dominates the time series at the beginning, but after about 15 days the subtidal frequency dominates. From the spectrum in figure 15(*b*) obtained by averaging spectra at the location and the surrounding eight grid points, we infer that the subharmonic frequency that gains energy is approximately $0.5\omega_0$. The subharmonic frequency in this case is, in fact, slightly stronger than the tidal frequency. Figure 15(*c*) quantifies the transfer of energy from the tidal frequency to the subtidal one, and shows how the spectrogram captures the conversion from tidal to subtidal motion and, then, back to tidal and, possibly, to the motion at other frequencies, near the end of the time series.

The instabilities occurring in a certain region form patches that spread spatially in a manner similar to that described by Teoh *et al.* (1997). Forced waves in the vicinity of instabilities are strong enough to affect surrounding regions, thus, the instability patches grow. Figure 16 demonstrates the development of the instability as in figure 15, but shows the contour plot of the velocity $\tilde{u}^n_{ij}$ in the lower 800 m of the water column as a function of z and t. It is seen that after about 1 day, a strong core with large horizontal velocities starts forming in the centre of the vertical cross-section. The core, alternating with frequency ω_0 becomes larger and after approximately 10 days, the core splits into two pieces, then into three, and so on. As the energy is injected into the region through the instability, the patch dominated

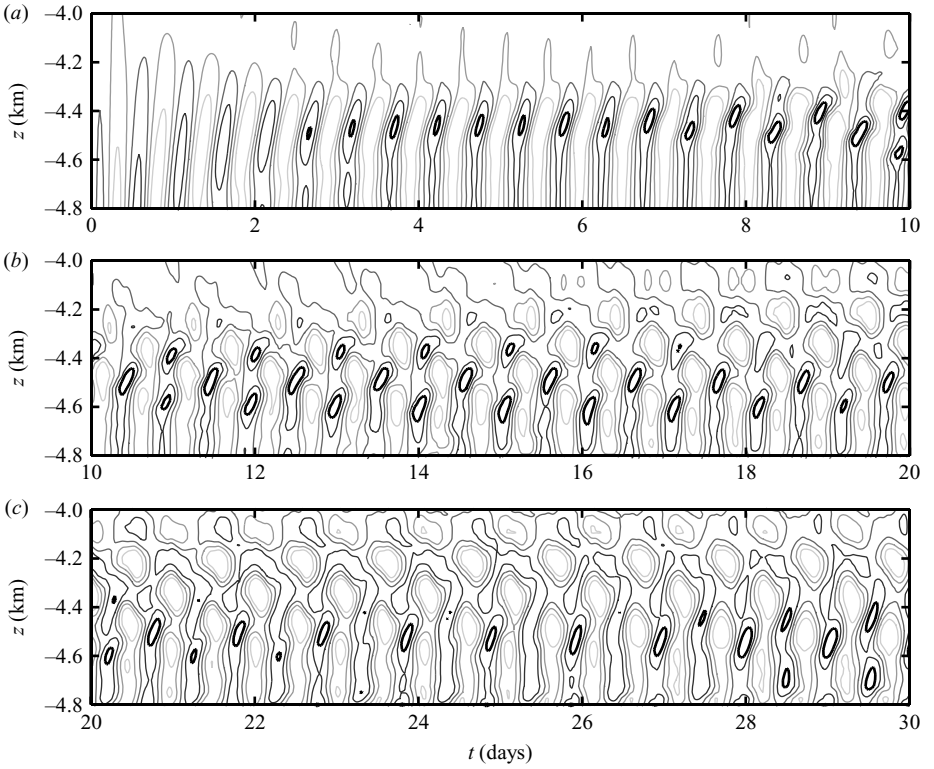

FIGURE 16. Contour plot of the horizontal velocity in the barotropic-Lagrangian reference frame for a vertical cross-section near the location $x = 15.7$ km and $z = -4.321$ km. Time intervals (*a*) [0, 10], (*b*) [10, 20] and (*c*) [20, 30] days.

by waves of subharmonic frequency is constantly expanding. Similar expansion of the instability patch is observed in other regions: for example, at a vertical cross-section near the point $(x, z) = (15.7, -4.321)$ km. This expansion is another factor that makes forced instabilities important: although the waves are not propagating from the vicinity of the instability, the region of instability is constantly growing and, thus, an overturning, which may eventually occur in the region, may affect regions as far as several kilometres from the centre of the instability.

4.7. *The cause of subharmonics*

The two strong subharmonics are generated by a parametric subharmonic instability, which in the fully nonlinear regime can be either a resonant or a non-resonant triad. When the strong subharmonics observed in the spectra are within the frequency range (f, N_b), their wavenumbers suggest resonant triad interactions. There are a discrete number of resonant triad interactions occurring in the highly nonlinear regions that generate the two strongest subharmonics. For example, in the case $\theta = 20^\circ$ N, there is one resonant triad corresponding to the destabilization of the tidal beam on top of the ridge and there is another corresponding to the instability on the side of the ridge. The instability of the internal tidal beam occurring on top of the ridge generates two subharmonic waves with frequencies ω_1 and ω_2 such that $\omega_1 + \omega_2 = \omega_0$. The two subharmonics are characterized by two distinct wavevectors: $\boldsymbol{K}_1 = (k_1, m_1)$ and $\boldsymbol{K}_2 = (k_2, m_2)$. The tidal beam, on the other hand, does not have any dominant

wavenumbers. The linear dispersion relation indicates that the sum combination of the wavevectors corresponding to the subharmonics on top of the ridge, i.e. $\boldsymbol{K}_1 + \boldsymbol{K}_2$, corresponds to the tidal frequency. Similarly, the two subharmonics generated on the side of the ridge are in resonance with the tidal beam.

Let us consider the example case $\theta = 20^\circ$ in more detail and estimate the dominant wavenumbers corresponding to the energetic subharmonic frequencies $\omega_1 = 0.43\omega_0$ and $\omega_2 = 0.57\omega_0$. The values of the subharmonic frequencies are obtained from the one-dimensional spectrum $\Upsilon(\omega)$. Apart from the wavenumbers corresponding to the subharmonics, we will also need to estimate the energetic wavenumbers characterizing the tidal beam.

The spatial distribution of the waves with a given frequency ω_α can be analysed using the following Fourier transform of the baroclinic velocities $\tilde{u}_{ij}^n$:

$$\chi_{ij}(\omega_\alpha) = \sum_{n=0}^{N-1} g_n \tilde{u}_{ij}^n \exp(-\mathrm{i}\omega_\alpha t_n), \tag{4.5}$$

where g_n is the same as for the spectral estimator $S_{ij}(\omega_\alpha)$. We consider the distribution $\chi_{ij}(\omega_\alpha)$ over the domain $\xi_{ij} \in [0, 40]$ km and restrict our attention to the three frequencies ω_1, ω_2 and ω_0. Note, that the transform $\chi_{ij}(\omega_\alpha)$ is the essential part of the direct spectral estimator $S_{ij}(\omega_\alpha)$; the two are related as follows: $S_{ij}(\omega_\alpha) = (\Delta t/\pi)|\chi_{ij}(\omega_\alpha)|^2$. As opposed to the spatial distribution $S_{ij}(\omega_\alpha)$, the transform $\chi_{ij}(\omega_\alpha)$ allows us to obtain the information about the relative phase of a wave at each coordinate (ξ_{ij}, η_{ij}). Using that information we can estimate the wavenumbers of a wave.

The phase field corresponding to frequency ω_α can be defined as follows:

$$\phi_{ij}(\omega_\alpha) = \mathrm{Im}\{\log(\chi_{ij}(\omega_\alpha))\},\ \phi_{ij}(\omega_\alpha) \in [-\pi, \pi], \tag{4.6}$$

where Im stands for the imaginary part. As the phase field ϕ_{ij} is discontinous and the phase itself is ambiguously defined, a better way to analyse the local phase of a wave is to consider either the real or imaginary part of the matrix $\chi_{ij}(\omega_\alpha)$ normalized by the absolute value of $\chi_{ij}(\omega_\alpha)$ at each point, e.g.

$$\varphi_{ij}(\omega_\alpha) = \mathrm{Re}\{\chi_{ij}(\omega_\alpha)\}/|\chi_{ij}(\omega_\alpha)|,\ \varphi \in [-1, 1], \tag{4.7}$$

where Re stands for the real part. Figure 17 demonstrates the phase fields $\varphi_{ij}(\omega_\alpha)$ for $\omega_\alpha = \omega_1$, ω_2 and ω_0. Lines of constant phase have the typical slope corresponding to the frequency of the wave. The actual distribution of each wave is much less regular than the phase field. To emphasize where the wave is most energetic, a contour of the field $|\chi_{ij}(\omega_\alpha)|$ is shown as a shaded patch on top of each of the phase fields.

The structure of the phase fields $\varphi_{ij}(\omega_1)$ and $\varphi_{ij}(\omega_2)$ shows that there are dominant wavenumbers for each subharmonic. However, as is seen in the field $\varphi_{ij}(\omega_1)$, the wavenumbers corresponding to the beams of subharmonic frequency emanating from the top of the ridge and from the side, are quite different. Accordingly, the distribution $\chi_{ij}(\omega_\alpha)$ has different wavenumbers: see, for example, the profile $\mathrm{Re}\{\chi_{ij}(\omega_1)\}$ at $\xi_{ij} = 11$ km and 30 km, shown in figure 18. On the other hand, the structure of the phase field corresponding to the wave of tidal frequency, i.e. $\varphi_{ij}(\omega_0)$, does not suggest any dominant wavenumbers.

To define the dominant vertical wavenumbers of the distribution $\chi_{ij}(\omega_\alpha)$, we apply a zero-padded discrete Fourier transform in the vertical for each index i. Thus, for each frequency, we obtain a distribution $\hat{\chi}(x, m)$ that shows the dominant wavenumbers.

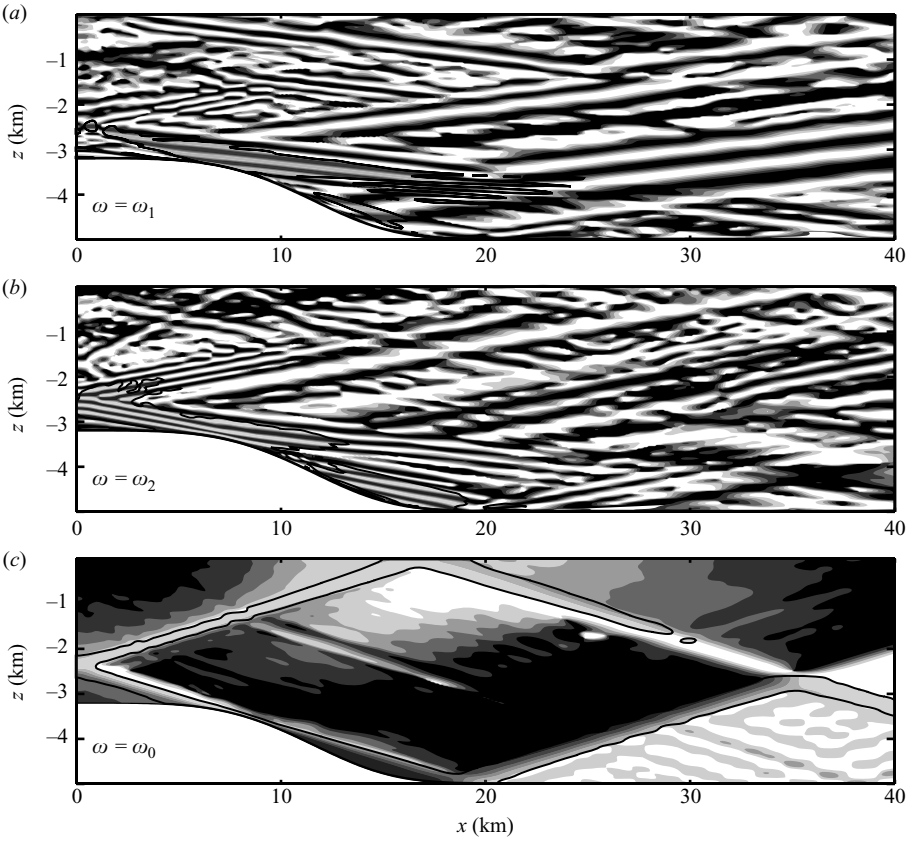

FIGURE 17. The phase fields φ_{ij} for the frequencies $\omega_1 = 0.4269\omega_0$, $\omega_2 = 0.5752\omega_0$ and ω_0 at latitude $\theta = 20^\circ$ N. The shading patches indicate the energetic regions for each case.

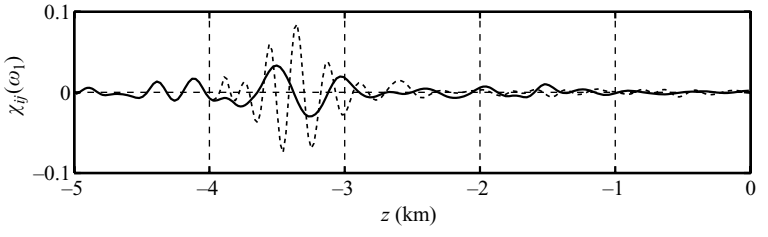

FIGURE 18. The profile $\chi_{ij}(\omega_1)$ for $\xi_{ij} = 11$ km (dashed line) and 30 km (solid line).

The signs of the wavenumbers obtained with this method are not necessarily correct and should be checked according to the direction in which the corresponding wave is propagating. Figure 19(a, b) shows the two fragments of the distribution $\hat{\chi}(x, m)$ with the two dominant vertical wavenumbers. One vertical wavenumber (m_1^{top}) corresponds to the instability on the top and another, to the instability on the side (m_1^{side}). Figure 19(c, d) shows the energetic wavenumbers for the frequency ω_2.

Figure 20 shows the distribution of the energetic wavenumbers of the waves of tidal frequency. The important difference in comparison with the case of subharmonics is that there are no localized peaks signifying dominant wavenumbers. Rather, the distribution of the energetic wavenumbers for the tidal frequency is decaying with

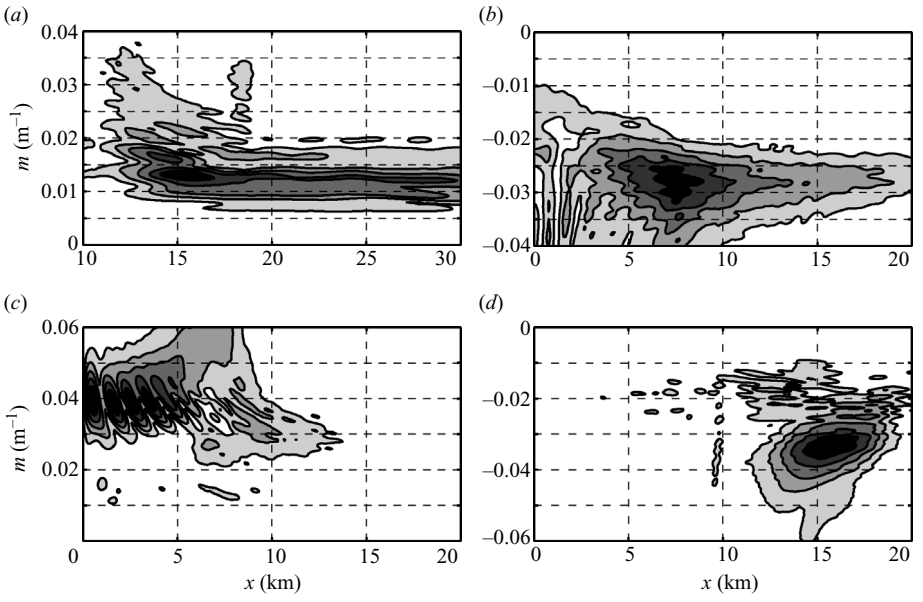

FIGURE 19. The distribution $\hat{\chi}_{ij}(x, m)$ at 20° N shown for: (*a*) frequency ω_1, positive wavenumbers, (*b*) frequency ω_1, negative wavenumbers, (*c*) frequency ω_2, positive wavenumbers, (*d*) frequency ω_2, negative wavenumbers. Black patches correspond to the maximum absolute values of $\hat{\chi}_{ij}(x, m)$.

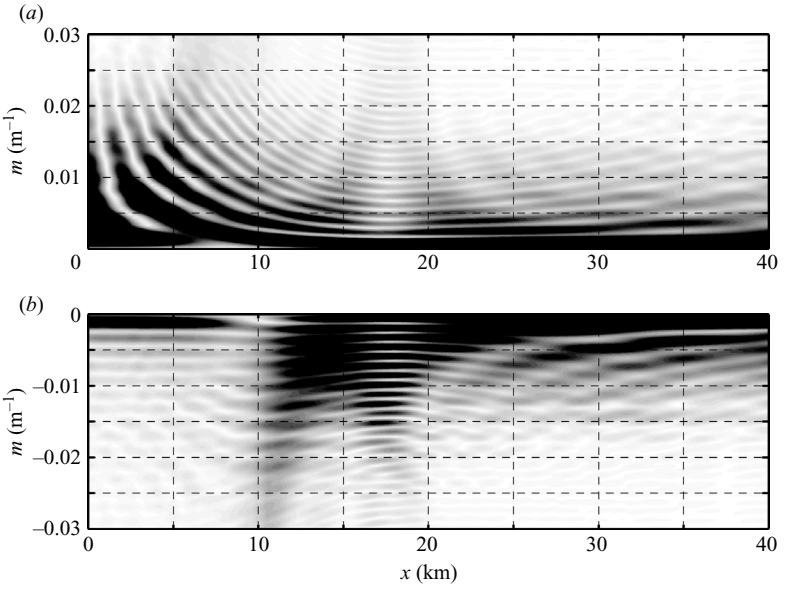

FIGURE 20. The distribution $\hat{\chi}_{ij}(x, m)$ at 20° N shown for frequency ω_0: (*a*) positive wavenumbers corresponding to the upward propagating beam, (*b*) negative wavenumbers corresponding to the downward propagating beam.

the vertical wavenumber. The pattern of the distribution reflects the fact that the upward propagating beam has more energy in high vertical wavenumbers in the region $0 \lessapprox x \lessapprox 10$ km, i.e. on top of the ridge. The downward propagating beam

Top	Side
$(k_1^{top}, m_1^{top}) = (-9.2765 \times 10^{-4}, -0.0277)\,\mathrm{m}^{-1}$	$(k_1^{side}, m_1^{side}) = (4.4205 \times 10^{-4}, -0.0132)\,\mathrm{m}^{-1}$
$(k_2^{top}, m_2^{top}) = (2.4937 \times 10^{-3}, 0.039)\,\mathrm{m}^{-1}$	$(k_2^{side}, m_2^{side}) = (-2.174 \times 10^{-3}, -0.034)\,\mathrm{m}^{-1}$

TABLE 2. Dominant wavenumbers of the resonant triads for the case 20° N.

has more energy in higher vertical wavenumbers in the region $10 \lessapprox x \lessapprox 20\,\mathrm{km}$, i.e. on the side of the ridge. The alternating black 'ribbons' in the distribution are the manifestation of what the vertical mode structure turns into over topography.

Once the dominant vertical wavenumber is found, the corresponding horizontal wavenumber can be constructed using the dispersion relation:

$$k = \pm m \sqrt{\frac{\omega^2 - f^2}{N_b^2 - \omega^2}}. \tag{4.8}$$

Table 2 gives the resulting wavenumbers for the two subharmonics. Note that the sign of the wavenumber m_1^{side} was corrected in accordance with the direction of the wave propagation. The waves characterized by $(\omega_1, k_1^{top}, m_1^{top})$ and $(\omega_2, k_2^{top}, m_2^{top})$ form a resonant triad with the wave $(\omega_0^{top}, k_0^{top}, m_0^{top}) = (\omega_1 + \omega_2, k_1^{top} + k_2^{top}, m_1^{top} + m_2^{top})$, where

$$\omega_0^{top} = \frac{\left(k_0^{top}\right)^2 N_b^2 + \left(m_0^{top}\right)^2 f^2}{\left(k_0^{top}\right)^2 + \left(m_0^{top}\right)^2} = 1.4591 \times 10^{-4}\,\mathrm{s}^{-1}. \tag{4.9}$$

Thus, within 5 % error, the frequency ω_0^{top} coincides with the tidal frequency ω_0 and, consequently, we conclude that the waves of frequencies ω_1 and ω_2 on top of the ridge form a resonant triad with the wave of tidal frequency. Similarly, it can be shown that the subharmonic waves on the side of the ridge form a difference resonant triad with the wave of tidal frequency, so that the corresponding frequency $\omega_0^{side} \approx 1.3426 \times 10^{-4}\,\mathrm{s}^{-1}$.

The dominant vertical wavenumbers of the subharmonics are very different along the top and sides of the topography. This is the reflection of the fact that, on the sides, the difference triad interaction takes place, whereas on the top, the dynamics is governed by the sum triad interaction.

5. Discussion

The fact that in some locations the flow is highly nonlinear results in subharmonic instability whose properties may be different from the properties of instabilities known from weakly nonlinear theory. As was shown in this paper, in the fully nonlinear regime, the instabilities may lead to generation of both progressive and forced waves. As the subharmonic instabilities play a major role in energy transfers occurring in a simplified system like ours and may potentially play a role in the ocean, some conceptions from the linear and weakly nonlinear theory should be reconsidered.

Using the term parametric subharmonic instability for the description of the main cause of the subharmonics can be confusing. Originally, when described within the weakly nonlinear framework, PSI was thought of as an instability acting on a single wave not perturbed by topography or coherent surrounding waves. This interpretation is misleading as the development of an instability in a violently perturbed wave, such

as one advected over topography, is much faster than in classical PSI. Also, PSI works only if the generated subharmonics are within the free-internal-wave frequency range (then PSI falls into the category of resonant-triad interactions). Identifying the main cause of subharmonics with PSI (what seems to be the case in the work by MacKinnon & Winters 2003, 2007), leads to a false conclusion that, once we go beyond the critical latitude where both subharmonics are forced, then there is no instability.

Forced internal waves seem to be underestimated or overlooked in comparison with progressive ones. The dispersion relation (1.1) from linear theory says that progressive internal waves are characterized by frequencies in the range (f, N_b), thus overlooking forced internal waves. The lack of attention to forced waves might be the consequence of the conception that resonant triad interactions, which can only produce waves within the range (f, N_b), are the dominant mechanism of energy transfers. However, according to Phillips (1967), 'there is no prior reason why forced components, whose wavenumbers and frequencies do not obey the wave-dispersion relation, should not be generated with amplitudes comparable with those of the primary waves.' In our runs, we have actually shown that non-resonant triad interactions can produce internal waves of comparable energies in the ranges $[0, f)$ and $(N_b, +\infty)$ (see, for example, figure 6). This feature of the energy transfers requires special attention, as the impact of forced waves on mixing can be even greater than that of progressive waves (Teoh *et al.* 1997). Trapped waves can accumulate energy more quickly and hence are more susceptible to overturning.

The last result we will discuss in this section is that the interharmonics in the spectrum are not a consequence of Doppler-shifted subharmonic frequencies, as was assumed, for example, in the work by Gerkema *et al.* (2006). Gerkema *et al.* (2006) investigated internal-tide generation at a continental shelf-break. They solved the non-hydrostatic equations for a time period of about 15 tidal periods, which is approximately a quarter of the time period that we use in our simulations. The spatial resolution in Gerkema *et al.* is close to ours: in the deep part of the domain (waterdepth 4 km), they use cells 100 m in the horizontal by 25 m in the vertical, whereas we use cells 100 m by 26.042 m. They also used strong damping in the form of a sponge layer to absorb baroclinic waves away from the source. Their kinetic energy spectra estimations are similar to ours, but have larger amount of leakage (mainly due to the short total model time); consequently, their estimations do not capture most of the interharmonics except for the strongest ones. For example, in the case of $\theta = 27.5^\circ$ N, their spectra have the interharmonic of the frequency $\omega = 0.5\omega_0$ and $\omega \approx 1.5\omega_0$. They suspected that the interharmonic frequency $1.5\omega_0$ was the result of the Doppler shift due to advection of the subharmonic waves by the tidal frequency waves. Our results suggest that the interharmonic frequencies observed in the spectrum are not a consequence of Doppler shifting. This follows from the comparison of spectra in the Eulerian, Lagrangian and barotropic-Lagrangian reference frames. Moreover, and here we return once again to the forced *vs.* progressive waves concept, the waves of subharmonic frequencies in the subinertial range are trapped waves localized in patches near the generation sites, whereas their counterparts, interharmonics separated from them by multiples of tidal frequency, are progressive internal waves manifested in internal wave beams.

6. Summary

Within our simplified model of tide–topography interaction, the energy cascade consists of the following main processes: (i) the barotropic tide losing energy to waves

of harmonic frequencies through the nonlinear mechanism described by Bell (1975) and Khatiwala (2003); (ii) PSI occurring in the tidal beam, which happens for all latitudes; (iii) the interaction of harmonics and subharmonics producing forced and progressive interharmonic waves at the combination frequencies. Once the spectral components are generated, energy starts 'trickling down' from the energetic waves toward weak ones.

Both harmonics $\{n\omega_0\}$ and interharmonics $\{\omega_\alpha + n\omega_0\}$, where $n \in \mathbb{N}$ and $\omega_\alpha \in (0, \omega_0]$, decay with n at a similar nearly exponential rate. As a result, the spectrum has a self-similar structure, which decays in magnitude at an exponential rate. This suggests a simple interpretation of the cascade that any spectral component $\omega_\beta \in (0, +\infty)$ present in the spectrum loses (by interacting with the wave of tidal frequency) the same fraction $\mu = \text{const}$ of its energy toward the spectral component $\omega_\beta + \omega_0$.

Investigation of the vertical scales of the internal wave fields revealed that among all the spectral components in the flow, subharmonics have the finest vertical scales and, thus, are the first candidates for direct mixing. Further investigation of vertical and horizontal wavenumber spectra showed that waves of subharmonic frequencies within the free internal wave range are generated through the PSI.

The instabilities are stronger for the near-critical latitudes; there, we observe strong waves of interharmonic frequencies. However, there is no sudden cutoff when the latitude becomes supercritical. For the latitude $\theta = 30^\circ$ N, which is slightly supercritical, some waves of subharmonic frequency are trapped. This suggests that the observed instabilities are of a forced non-resonant type. Instabilities of the forced non-resonant type also generate subharmonic frequencies in the case $\theta = 40^\circ$ N.

Previously, attention has focused on harmonics and strong subharmonics only. Interharmonics, ignited by instabilities in the highly nonlinear regions, and multiplied through triad interactions, represent the next logical step in understanding the process of energy cascade in internal waves.

This work was supported by a Research Network Grant (CLIVAR) funded by the Natural Sciences and Engineering Research Council and the Canadian Foundation for Climate and Atmospheric Science.

REFERENCES

Bell, J. B., Collela, P. & Glaz, H. M. 1989 A second-order projection method for the incompressible Navier–Stokes equations. *J. Comput. Phys.* **85**, 257–283.

Bell, J. B. & Marcus, D. L. 1992 A second-order projection method for variable-density flows. *J. Comput. Phys.* **101**, 334–348.

Bell, J. B., Solomon, J. M. & Szymczak, W. G. 1989 A second-order projection method for the incompressible Navier–Stokes equations on quadrilateral grids. In *AIAA 9th Computational Fluids Dynamics Conference*. American Institute of Aeronautics and Astronautics, Buffalo, New York.

Bell, T. 1975 Lee waves in stratified flows with simple harmonic time dependence. *J. Fluid Mech.* **67**, 705–722.

Carter, G. S. & Gregg, M. C. 2006 Persistent near-diurnal internal waves observed above a site of M2 barotropic-to-baroclinic conversion. *J. Phys. Oceanogr.* **36**, 1136–1147.

Carter, G. S., Gregg, M. C. & Merrifield, M. A. 2006 Flow and mixing around a small seamount on Kaena Ridge, Hawaii. *J. Phys. Oceanogr.* **36**, 1036–1052.

Chashechkin, Yu. D. & Nekludov, V. I. 1990 Nonlinear interaction of bundles of short two-dimensional monochromatic internal waves in an exponentially stratified liquid. *Dokl. Earth Sci. Sect.* **311**, 235–238.

Cooley, J. W. & Tukey, J. W. 1965 An algorithm for the machine computation of complex fourier series. *Math. Comput.* **19**, 297–301.

Dewar, W. K., Bingham, R. J., Iverson, R. L., Nowacek, D. P., Laurent, L. C. St & Wiebe, P. H. 2006 Does the marine biosphere mix the ocean? *J. Mar. Res.* **64**, 541–561.

Drazin, P. G. 1977 On the instability of an internal gravity wave. *Proc. R. Soc. Lond.* A **356**, 411–432.

Furuchi, N., Hibiya, T. & Niwa, Y. 2005 Bispectral analysis of energy transfer within the two-dimensional oceanic internal wave field. *J. Phys. Oceanogr.* **35**, 2104–2109.

Furue, R. 2003 Energy transfer within the small-scale oceanic internal wave spectrum. *J. Phys. Oceanogr.* **33**, 267–282.

Garrett, C. 2003 Mixing with latitude. *Nature* **422**, 477–478.

Garrett, C. & Munk, W. 1975 Space–time scales of internal waves: a progress report. *J. Geophys. Res.* **80**, 291–297.

Gerkema, T., Staquet, C. & Bouruet-Aubertot, P. 2006 Decay of semi-diurnal internal-tide beams due to subharmonic resonance. *Geophys. Res. Lett.* **33** (L08604).

Görtler, H. 1943 Uber eine schwingungserscheinung in flussigkeiten mit stabiler dichteschichtung. *Z. Angew. Math. Mech.* **23**, 65.

van Haren, H., Maas, L. & van Aken, H. 2002 On the nature of internal wave spectra near a continental slope. *Geophys. Res. Lett.* **29** (12).

Hasselman, K. 1967 A criterion for nonlinear wave stability. *J. Fluid Mech.* **30**, 737–739.

Hibiya, T., Niwa, Y. & Fujiwara, K. 1998 Numerical experiments of nonlinear energy transfer within the oceanic internal wave spectrum. *J. Geophys. Res.* **103** (C9), 18 715–18 722.

Holloway, G. 1980 Oceanic internal waves are not weak waves. *J. Phys. Oceanogr.* **10**, 906–914.

Holloway, P. E. & Merrifield, M. A. 1999 Internal tide generation by seamounts, ridges and islands. *J. Geophys. Res.* **104**, 937–951.

Javam, A., Imberger, J. & Armfield, S. W. 1999 Numerical study of internal wave reflection from sloping boundaries. *J. Fluid Mech.* **396**, 183–201.

Javam, A., Imberger, J. & Armfield, S. W. 2000 Numerical study of internal wave–wave interactions in a stratified fluid. *J. Fluid Mech.* **415**, 65–87.

Khatiwala, S. 2003 Generation of internal tides in an ocean of finite depth: analytical and numerical calculations. *Deep-Sea Res.* **50**, 3–21.

Kistovich, A. V. & Chashechkin, Yu. D. 1991 Nonlinear interaction of two-dimensional packets of monochromatic internal waves. *Izv. Atmos. Ocean Phys.* **27**, 946–951.

Koudella, C. R. & Staquet, C. 2006 Instability mechanisms of a two-dimensional progressive internal gravity wave. *J. Fluid Mech.* **548**, 165–196.

Kundu, P. & Cohen, I. M. 2002 *Fluid Mechanics*, 2nd edn. Elsevier.

Lamb, K. G. 1994 Numerical experiments of internal wave generation by strong tidal flow across a finite amplitude bank edge. *J. Geophys. Res.* **99**, 843–864.

Lamb, K. G. 2004 Nonlinear interaction among internal wave beams generated by tidal flow over supercritical topography. *Geophys. Res. Lett.* **31** (L09313).

Legg, S. & Huijts, K. M. H. 2006 Preliminary simulations of internal waves and mixing generated by finite amplitude tidal flow over isolated topography. *Deep-Sea Res. II* **53**, 140–156.

McEwan, A. D. 1971 Degeneration of resonantly excited standing internal gravity waves. *J. Fluid Mech.* **50**, 431–448.

McEwan, A. D. 1973 Interactions between internal gravity waves and their traumatic effect on a continuous stratification. *Boundary-Layer Met.* **5**, 159–175.

MacKinnon, J. A. & Winters, K. B. 2003 Spectral evolution of bottom-forced internal waves. In *Proc. 13th 'Aha Huliko'a Hawaiian Winter Workshop*, pp. 73–83.

MacKinnon, J. A. & Winters, K. B. 2007 Tidal mixing hotspots governed by rapid parametric subharmonic instability. *J. Phys. Oceanogr.* (submitted).

Martin, J. P. & Rudnick, D. L. 2007 Inferences and observations of turbulent dissipation and mixing in the upper ocean at the Hawaiian Ridge. *J. Phys. Oceanogr.* **37**, 476–494.

Martin, J. P., Rudnick, D. L. & Pinkel, R. 2006 Spatially broad observations of internal waves in the upper ocean at the Hawaiian Ridge. *J. Phys. Oceanogr.* **36**, 1085–1103.

Mowbray, D. E. & Rarity, B. S. H. 1967 A theoretical and experimental investigation of the phase configuration of internal waves of small amplitude in a density stratified fluid. *J. Fluid Mech.* **28**, 1–16.

Munk, W. & Wunsch, C. 1998 Abyssal recipes II: energetics of tidal and wind mixing. *Deep-Sea Res.* **45**, 1977–2010.

Nansen, F. 1902 Oceanography of the North Polar Basin. The Norwegian north polar expedition 1893–96. *Scientific Results* (9).

Olbers, D. 1983 Models of the oceanic internal wave field. *Rev. Geophys. Space Phys.* **21**, 1567–1606.

Olbers, D. & Pomphrey, N. 1981 Disqualifying two candidates for the energy balance of oceanic internal waves. *J. Phys. Oceanogr.* **11**, 1423–1425.

Orlanski, I. 1981 Energy transfer among internal gravity modes: weak and strong interactions. *J. Geophys. Res.* **86**, 4103–4124.

Peacock, T. & Tabaei, A. 2005 Visualization of nonlinear effects in reflecting internal wave beams. *Phys. Fluids* **17** (061702).

Percival, D. B. & Walden, A. T. 1993 *Spectral Analysis for Physical Applications: Multitaper and Conventional Univariate Techniques*. Cambridge University Press.

Phillips, O. M. 1967 Theoretical and experimental studies of gravity wave interactions. *Proc. R. Soc. Lond.* **299**, 104–119.

Phillips, O. M. 1977 *The Dynamics of the Upper Ocean*, 2nd edn. Cambridge University Press.

Pingree, R. D. & New, A. L. 1991 Abyssal penetration and bottom reflection of internal tidal energy in the bay of biscay. *J. Phys. Oceanogr.* **21**, 28–39.

Rainville, L. & Pinkel, R. 2006 Baroclinic energy flux at the Hawaiian Ridge: observations from the r/p flip. *J. Phys. Oceanogr.* **36**, 1104–1122.

de Silva, I. P. D., Imberger, J. & Ivey, G. N. 1997 Localized mixing due to a breaking internal wave ray at a sloping bed. *J. Fluid Mech.* **350**, 1–27.

Staquet, C. & Sommeria, J. 2002 Internal gravity waves: from instabilities to turbulence. *Annu. Rev. Fluid Mech.* **34**, 559–593.

Stashchuk, N. & Vlasenko, V. 2005 Topographic generation of internal waves by nonlinear superposition of tidal harmonics. *Deep-Sea Res. I* **52**, 605–620.

Sverdrup, H. U., Johnson, M. W. & Fleming, R. H. 1942 *The Oceans: their Physics, Chemistry, and General Biology*. Prentice-Hall.

Tabaei, A., Akylas, T. R. & Lamb, K. G. 2005 Nonlinear effects in reflecting and colliding internal wave beams. *J. Fluid Mech.* **526**, 217–243.

Teoh, S. G., Ivey, G. N. & Imberger, J. 1997 Experimental study of two intersecting internal waves. *J. Fluid Mech.* **336**, 91–122.

Thorpe, S. A. 1968 On the shape of progressive internal waves. *Phil. Trans. R. Soc. Lond.* A **263**, 563–614.

Winters, K. B. & D'Asaro, E. A. 1997 Direct simulation of internal wave energy transfer. *J. Phys. Oceanogr.* **27**, 1937–1945.

Zhang, H. P., King, B. & Swinney, H. L. 2007 Experimental study of internal gravity waves generated by supercritical topography. *Phys. Fluids* **19**, 096602.